

# The *Swift*/*Fermi* GRB 080928 from 1 eV to 150 keV

A. Rossi<sup>1</sup>, S. Schulze<sup>1,2</sup>, S. Klose<sup>1</sup>, D. A. Kann<sup>1</sup>, A. Rau<sup>3</sup>, H. A. Krimm<sup>4</sup>, G. Jóhannesson<sup>5</sup>, A. Panaitescu<sup>6</sup>, F. Yuan<sup>7</sup>, P. Ferrero<sup>1,8,9</sup>, T. Krühler<sup>3,10</sup>, J. Greiner<sup>3</sup>, P. Schady<sup>3</sup>, S. B. Pandey<sup>7,11</sup>, L. Amati<sup>12</sup>, P. M. J. Afonso<sup>3,\*</sup>, C. W. Akerlof<sup>7</sup>, L. A. Arnold<sup>13</sup>, C. Clemens<sup>3</sup>, R. Filgas<sup>3</sup>, D. H. Hartmann<sup>14</sup>, A. Küpcü Yoldaş<sup>3,15</sup>, S. McBreen<sup>3,16</sup>, T. A. McKay<sup>7</sup>, A. Nicuesa Guelbenzu<sup>1</sup>, F. Olivares E.<sup>3</sup>, B. Paciesas<sup>17</sup>, E. S. Rykoff<sup>18</sup>, G. Szokoly<sup>3,19</sup>, A. C. Updike<sup>14</sup>, and A. Yoldaş<sup>15</sup>

<sup>1</sup> Thüringer Landessternwarte Tautenburg, Sternwarte 5, D-07778 Tautenburg, Germany

<sup>2</sup> Centre for Astrophysics and Cosmology, Science Institute, University of Iceland, Dunhagi 5, IS-107 Reykjavík, Iceland

<sup>3</sup> Max-Planck-Institut für Extraterrestrische Physik, Giessenbachstraße, D-85748 Garching, Germany

<sup>4</sup> CRESST, Universities Space Research Association and NASA GSFC, Greenbelt, MD 20771, USA

<sup>5</sup> Hansen Experimental Physics Laboratory, Stanford University, Stanford, CA 94305, USA

<sup>6</sup> ISR-1, Los Alamos National Laboratory, Los Alamos, NM 87545, USA

<sup>7</sup> Physics Department, University of Michigan, Ann Arbor, MI 48109, USA

<sup>8</sup> Instituto de Astrofísica de Canarias (IAC), E-38200 La Laguna, Tenerife, Spain

<sup>9</sup> Departamento de Astrofísica, Universidad de La Laguna (ULL), E-38205 La Laguna, Tenerife, Spain

<sup>10</sup> Universe Cluster, Technische Universität München, Boltzmannstraße 2, D-85748, Garching, Germany

<sup>11</sup> ARIES, Manora Peak, Nainital, Uttarakhand, India, 263129

<sup>12</sup> INAF/IASF Bologna, Via Gobetti 101, I-40129 Bologna, Italy

<sup>13</sup> University of Rochester, Department of Physics and Astronomy, Rochester, NY 14627-0171, USA

<sup>14</sup> Clemson University, Department of Physics and Astronomy, Clemson, SC 29634-0978, USA

<sup>15</sup> Institute of Astronomy, University of Cambridge, Madingley Road, CB3 0HA, Cambridge, UK

<sup>16</sup> School of Physics, University College Dublin, Dublin 4, Republic of Ireland

<sup>17</sup> University of Alabama in Huntsville, NSSTC, 320 Sparkman Drive, Huntsville, AL 35805, USA

<sup>18</sup> Physics Department, University of California at Santa Barbara, 2233B Broida Hall, Santa Barbara, CA 93106, USA

<sup>19</sup> Institute of Physics, Eötvös University, Pázmány P. s. 1/A, 1117 Budapest, Hungary

Received: 1 July 2010; accepted XXXX

## ABSTRACT

We present the results of a comprehensive study of the Gamma-Ray Burst 080928 and of its afterglow. GRB 080928 was a long burst detected by *Swift*/BAT and *Fermi*/GBM. It is one of the exceptional cases where optical emission was already detected when the GRB itself was still radiating in the gamma-ray band. For nearly 100 seconds simultaneous optical, X-ray and gamma-ray data provide a coverage of the spectral energy distribution of the transient source from about 1 eV to 150 keV. In particular, we show that the SED during the main prompt emission phase is in agreement with synchrotron radiation. We construct the optical/near-infrared light curve and the spectral energy distribution based on *Swift*/UVOT, ROTSE-IIIa (Australia) and GROND (La Silla) data and compare it to the X-ray light curve retrieved from the *Swift*/XRT repository. We show that its bumpy shape can be modeled by multiple energy injections into the forward shock. Furthermore, we investigate if the temporal and spectral evolution of the tail emission of the first strong flare seen in the early X-ray light curve can be explained by large-angle emission (LAE). We find that a non-standard LAE model is required to explain the observations. Finally, we report on the results of our search for the GRB host galaxy, for which only a deep upper limit can be provided.

**Key words.** Gamma rays: bursts: individual: GRB 080928

## 1. Introduction

Currently there is a golden age in Gamma-Ray Burst (GRB) research. The dedicated *Swift* gamma-ray satellite was successfully launched in November 2004 (Gehrels et al. 2004), and is in continuous operation for more than 5 years now. Its sophisticated Burst Alert Telescope (BAT; Barthelmy et al. 2005), covering 15 to 150 keV, detects about 100 GRBs per year with 3 arcmin localization accuracy (see J. Greiner's Internet page at <http://www.mpe.mpg.de/~jcgrbgen.html>). In addition, about once per month the European INTEGRAL gamma-ray satellite (Winkler et al. 2003), usually pointing towards pre-

planned targets for days or weeks, localizes a GRB with similar position accuracy (see Vianello et al. 2009). Also the Italian AGILE high-energy satellite (Tavani et al. 2009) contributes about a handful of burst detections and localizations per year (e.g., Giuliani et al. 2008; Rossi et al. 2008b). Thanks to *Swift*'s rapid and autonomous slewing capabilities, in combination with its highly sensitive X-ray telescope (XRT; Burrows et al. 2005a) as well as its optical/UV telescope (UVOT; Roming et al. 2005), about 50 to 70 GRB optical afterglows can be localized annually, with 30 to 40 having redshifts determined.

Roughly four years after *Swift*'s launch the *Fermi* Gamma-Ray Space Telescope was launched into orbit (June 2008). Its Gamma-Ray Burst Monitor (GBM; Meegan et al. 2009) and Large Area Telescope (LAT; Atwood et al. 2009) cover an unprecedentedly wide energy range from 8 keV to 300 GeV. Up to

Send offprint requests to: A. Rossi, [rossi@tls-tautenburg.de](mailto:rossi@tls-tautenburg.de)

\* Present address: American River College, Physics Department, 4700 College Oak Drive, Sacramento, CA 95841, USA

the end of November 2010, LAT has localized 17 GRBs to positions of less than a degree in error, of these, eight have optical afterglows and redshifts<sup>1</sup>. Furthermore, a larger number of *Swift* GRBs have also been detected by *Fermi*/GBM, allowing a more thorough investigation of the prompt emission above 150 keV.

Here we report on the analysis of the prompt gamma-ray emission and the afterglow of GRB 080928, as well as on the search for its host galaxy. This burst was detected by *Swift*/BAT and *Fermi*/GBM but not seen by *Fermi*/LAT. Its afterglow was rapidly found, and Vreeswijk et al. (2008) reported a redshift of  $z = 1.692$ . The burst is of particular interest since optical as well as X-ray emission was detected by *Swift*/UVOT and *Swift*/XRT, respectively, when the GRB was still radiating in the gamma-ray band. This makes it one of a rare number of cases (e.g., GRBs 041219A, 050820A, 051111, 061121; Shen & Zhang 2009), where a broad-band spectral energy distribution (SED) from about 1 eV to 150 keV can be constructed for the prompt emission phase.

Throughout this paper we adopt a world model with  $H_0 = 71$  km s<sup>-1</sup> Mpc<sup>-1</sup>,  $\Omega_M = 0.27$ ,  $\Omega_\Lambda = 0.73$  (Spergel et al. 2003). For the flux density of the afterglow we use the usual convention  $F_\nu(t) \propto t^{-\alpha} \nu^{-\beta}$ .

## 2. Data and analysis

### 2.1. *Swift*/BAT and *Fermi*/GBM data

The long burst GRB 080928 triggered the Burst Alert Telescope of *Swift* at  $t_0 = 15:01:32.86$  UT (Sakamoto et al. 2008) on the 28th of September 2008. This was an image trigger lasting 112 seconds. The prompt emission detected in the BAT began with a faint precursor at  $t_0 - 90$  s, then weak emission starting at  $t_0 - 20$  s and lasting for 40 s, followed by a second, slightly brighter peak starting at 50 s and ending at 120 s after the trigger (Fig. 1). The main emission of the GRB started at  $t_0 + 170$  seconds, with two peaks at 204 and 215 seconds<sup>2</sup>. Another less significant peak is detected around 310 s before fading out to at least 400 seconds when *Swift* had to stop observing due to its entry into the South Atlantic Anomaly (SAA) and the noise level became too large for any late emission to be detected in the BAT (Cummings et al. 2008; Fenimore et al. 2008; Sakamoto et al. 2008).

The main burst emission also triggered the Gamma-Ray Burst Monitor onboard *Fermi* (Paciesas et al. 2008), while the INTEGRAL satellite was passing through the SAA during the time of GRB 080928 and thus could not observe the burst with the anti-coincidence shield of the spectrometer SPI (SPI-ACS, Rau et al. 2005). GBM consists of 12 sodium iodide (NaI) detectors which cover the energy band between 8 keV and 1 MeV, and two bismuth germanate (BGO) scintillators which are sensitive at energies between 150 keV and 40 MeV. Emission from the burst was predominately seen in the NaI detectors. The GBM light curve (Fig. 1) shows a single pulse corresponding to the emission maximum observed by *Swift* at

$$t_{0,\text{GBM}} = t_0 + 204 \text{ s}. \quad (1)$$

We analyzed data collected by BAT between  $t_0 - 239$  s and  $t_0 + 494$  s in event mode with 100  $\mu$ s time resolution and about 6 keV energy resolution. The data were processed using standard BAT analysis tools, and a background-subtracted light curve was

produced using the tool *batmaskwtevt* with the best source position. For spectral analysis, the data were binned so that the signal-to-noise ratio was at least 3.0. During the main peak, the bin edges were chosen to match the *Swift*/XRT spectral bins. The spectra were fit using *Xspec v12.5.0*.

The spectral analysis of the *Fermi* data was performed with the software package *RMFIT v3.2rc1* using Castor statistics. Here, we analyzed the GBM spectra of the brightest four NaI detectors (#0, #3, #4 & #7) for two different integration windows, one covering the broad emission maximum from  $t_{0,\text{GBM}} - 5.248$  s to  $t_{0,\text{GBM}} + 24.448$  s while the second was constrained to  $\approx 4$  s around the peak ( $t_{0,\text{GBM}} - 1.152$  s to  $t_{0,\text{GBM}} + 2.944$  s). The variable GBM background was subtracted for all detectors individually by fitting an energy-dependent, third-order polynomial to the background data. The background interval used for the analysis was from  $t_{0,\text{GBM}} - 100$  s to  $t_{0,\text{GBM}} - 50$  s and from  $t_{0,\text{GBM}} + 100$  s to  $t_{0,\text{GBM}} + 350$  s. We used the standard 128 energy bins of the CSPEC data-type, using the channels above 8 keV of the NaIs, and ignoring the so-called overflow channels.

### 2.2. *Swift*/XRT data

*Swift*/XRT started to observe the BAT GRB error circle 170 seconds after the trigger and found an unknown X-ray source at coordinates R.A. (J2000) = 6<sup>h</sup>20<sup>m</sup>16<sup>s</sup>.87, Dec. = -55°11'58".5, with a final uncertainty of 1'.4 (Osborne et al. 2008; Sakamoto et al. 2008). Observations continued until 2.7 days after the GRB, when the source became too faint to be detected.

We obtained the X-ray data from the *Swift* data archive and the light curve from the *Swift* light curve repository (Evans et al. 2007, 2009). To reduce the data, the software package *HeaSoft* 6.6.1 was used<sup>3</sup> with the calibration file version v011<sup>4</sup>. Data analysis was performed following the procedures described in Nousek et al. (2006). We found that the X-ray emission was only sufficiently bright to perform a spectral analysis in the first two observing blocks (000–001). However, the early windowed timing (wt) mode and photon counting (pc) mode data were highly affected by pile-up. To account for this effect, we applied the methods presented in Romano et al. (2006) and Vaughan et al. (2006).

Due to the brightness of the source in wt mode, a time filter was defined to have at least 500 counts (background-subtracted) for every spectrum. In pc mode the average number of counts per spectrum is 300 due to pile-up. On these spectra  $\chi^2$ -statistics were applied. The spectrum we obtained from observing block 001 has only 102 counts (background-subtracted). Therefore, we could only apply *Cash* statistics (Cash 1979; Evans et al. 2009). In total, from both observing blocks we extracted the SED for 27 epochs, covering 1.4 days.

Following Butler & Kocevski (2007), we initially fitted the pc-mode spectra with an absorbed power-law to obtain  $N_{\text{H}}^{\text{host}}$  using *Xspec v12.5.0*. This model consists of two absorption components, one in the host frame and another one in the Galaxy. For both absorbers we used the Tübingen abundance template by Wilms et al. (2000), with the Galactic absorption fixed to  $N_{\text{H}}^{\text{Gal}} = 0.56 \times 10^{21}$  cm<sup>-2</sup> (Kalberla et al. 2005). The spectra were then fitted in two steps. First, all pc-mode spectra of the XRT observing block 000 were stacked using the *FTOOL mathpha* (Blackburn 1995)<sup>5</sup>. This spectrum contained about 1000 counts. The fitted absorbed power-law is characterized by a spectral

<sup>1</sup> <http://fermi.gsfc.nasa.gov/ssc/observations/types/grbs/grb-table/>

<sup>2</sup> If not stated otherwise, for the rest of the paper all times refer to the zero-point  $t_0$ .

<sup>3</sup> <http://heasarc.gsfc.nasa.gov/docs/software/lheasoft>

<sup>4</sup> [heasarc.gsfc.nasa.gov/docs/heasarc/caldb/swift](http://heasarc.gsfc.nasa.gov/docs/heasarc/caldb/swift)

<sup>5</sup> <http://heasarc.gsfc.nasa.gov/ftools/>

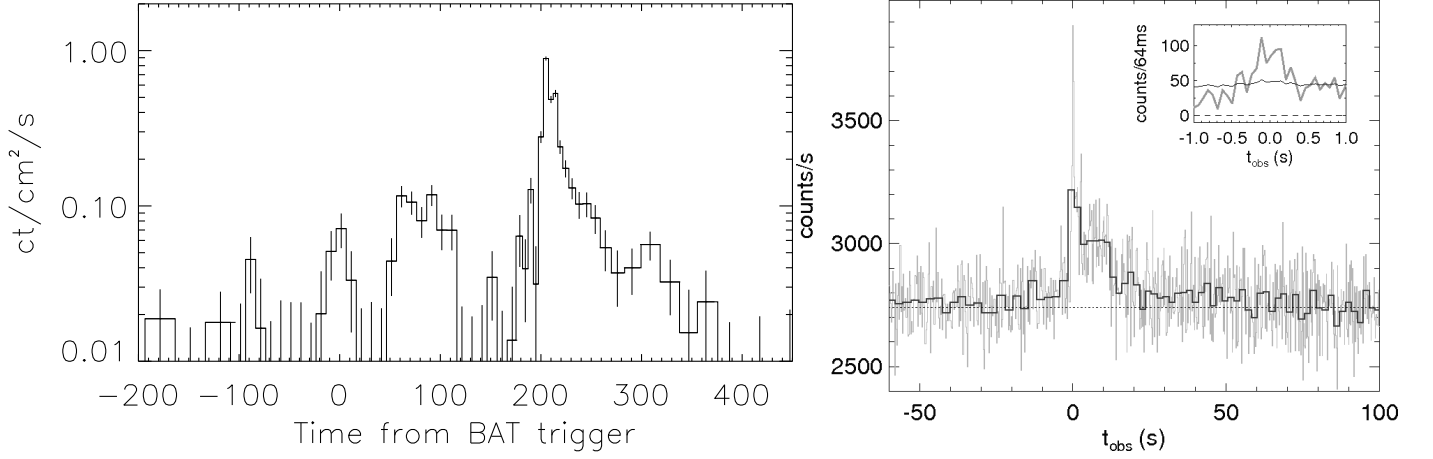


**Fig. 1.** *Left:* The light curve of GRB 080928 as seen by *Swift*/BAT. *Swift* triggered at the gamma-ray peak at  $t_0 = 0$  which was followed by at least two further peaks with the maximum at  $t_0 + 204$  s. There may be a faint precursor of the main burst at  $t_0 - 90$  s. *Right:* *Fermi*/GBM light curve of the NaI detectors #0, #3, #4 & #7 combined with 2 s resolution (black line) and 0.256 s resolution (gray line). A zoom into the 64 ms-binned, background-subtracted light curve around the peak is shown in the inset. Variability on time scales of  $\sim 128$  ms is detected at  $3\sigma$  (solid gray line) above the background plus shot noise fluctuations. Note that in this figure the time zero-point is the *Fermi*/GBM trigger time  $t_{0,\text{GBM}}$  (Eq. 1).

slope of  $\beta_X = 1.09^{+0.07}_{-0.10}$  and an effective hydrogen column density of  $N_{\text{H}}^{\text{host}} = 3.6^{+1.8}_{-2.2} \times 10^{21} \text{ cm}^{-2}$ . The spectral slope agrees with the observed mean value of  $\beta_X \sim 1$  found by, e.g., Racusin et al. (2009) and Evans et al. (2009). Having derived  $N_{\text{H}}^{\text{host}}$  in this way, the early spectra (wt-data) were fitted with an absorbed power-law in which  $N_{\text{H}}^{\text{host}}$  was fixed to the previously derived value.

### 2.3. Optical/NIR data

*Swift*/UVOT started observing about 3 min after the trigger, still before the onset of the main emission of the GRB, and immediately found an optical afterglow candidate (Kuin et al. 2008; Sakamoto et al. 2008). The redshift reported by Vreeswijk et al. (2008) was later refined to  $z = 1.6919$  by Fynbo et al. (2009).<sup>6</sup>

*Swift*/UVOT data were analyzed using the standard analysis software distributed within FTOOLS, version 6.5.1. For all the detections, the source count rates were extracted within a  $3''$  aperture. An aperture correction was estimated from selected nearby point sources in each exposure and applied to obtain the standard UVOT photometry calibrated for a  $5''$  aperture.

Ground-based follow-up observations were performed by our group using the ROTSE-IIIa 0.45m telescope in Australia (Rykoff et al. 2008) and the MPG/ESO 2.2m telescope on La Silla, Chile, equipped with the multi-channel imager GROND (Greiner et al. 2007, 2008). This data set (Tables A.1, A.3; Fig. A.1) was supplemented by data published from the VLT (Vreeswijk et al. 2008; Fynbo et al. 2009), and the 16'' Watcher telescope in South Africa (Ferrero et al. 2008).

ROTSE-IIIa data were analyzed using a PSF photometry package based on DAOPHOT following the procedure described in Quimby et al. (2006). GROND optical/NIR data were analyzed through standard PSF photometry using DAOPHOT tasks under IRAF (Tody 1993) similar to the procedure described in Krühler et al. (2008). Aperture photometry was ap-

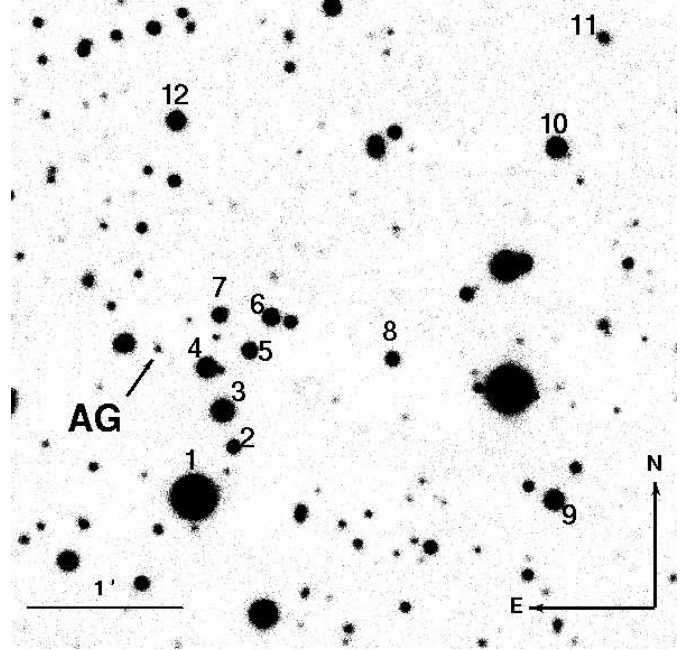


**Fig. 2.** Finding chart of the afterglow of GRB 080928 (GROND  $i'$  band, at 0.603 days after the burst). The afterglow (AG) and the secondary photometric standards used (Table A.4) are indicated.

plied when analyzing the field galaxies, using the DAOPHOT package (Warmels 1992). Afterglow coordinates were derived from the GROND 3rd epoch  $g'r'i'z'$ -band data. The stacked image has an astrometric precision of about  $0''.3$ , corresponding to the RMS accuracy of the USNO-B1 catalogue (Monet et al. 2003). The coordinates of the optical afterglow (Fig. 2) are R.A. (J2000) =  $06^{\text{h}}20^{\text{m}}16^{\text{s}}.83$ , Dec. =  $-55^{\circ}11'58''.9$  (Galactic coordinates  $l, b = 263^{\circ}82', -26^{\circ}31'$ ). Magnitudes were corrected for Galactic extinction using the interstellar extinction curve derived by Cardelli et al. (1989) and by assuming  $E(B - V) = 0.07$  mag (Schlegel et al. 1998) and a ratio of total-to-selective extinction of  $R_V = 3.1$ .

<sup>6</sup> For this redshift the distance modulus is  $m - M = 45.54$  mag, the luminosity distance  $3.95 \times 10^{28}$  cm, the look-back time 9.76 Gyr (3.91 Gyr after the Big Bang), and 1 arcsec on the sky corresponds to a projected distance of 8.56 kpc.

**Table 1.** Spectral fit results for *Swift*/BAT and the *Fermi*/GBM NaI detectors #0,3,4,7.

instrument	model	$\tilde{\beta}_1$	$E_1$	$\tilde{\beta}_2$	$E_2$	$\tilde{\beta}_3$	$\chi^2/\text{d.o.f.}$	$F_{\text{ph}} (0.3-1)$	$F_{\text{ph}} (0.3-10)$
<b>46.5 s &lt; <math>t_0</math> &lt; 121.0 s</b>									
BAT-GBM	db-pl	—	$12.37^{+1.52}_{-12.37}$	$1.92^{+0.13}_{-0.18}$	$143^{+37}_{-64}$	—	582 / 560	—	—
<b>202.848 s &lt; <math>t_0</math> &lt; 206.944 s = -1.152 s &lt; <math>t_{0,\text{GBM}}</math> &lt; 2.944 s</b>									
GBM	s-pl	—	—	$1.75 \pm 0.04$	—	—	422 / 438	$0.131 \pm 0.004$	$0.21 \pm 0.06$
GBM	Band	—	—	$1.24 \pm 0.16$	$108 \pm 24$	$3.3 \pm 4.6$	411 / 436	$0.07 \pm 0.02$	$0.09 \pm 0.02$
XRT-BAT-GBM	db-pl	$0.62^{+0.10}_{-0.18}$	$3.94^{+0.56}_{-0.62}$	$1.74^{+0.05}_{-0.08}$	$131^{+6}_{-16}$	—	639 / 581	—	—
<b>198.752 s &lt; <math>t_0</math> &lt; 228.448 s = -5.248 s &lt; <math>t_{0,\text{GBM}}</math> &lt; 24.448 s</b>									
GBM	s-pl	—	—	$1.90 \pm 0.04$	—	—	571 / 438	$0.035 \pm 0.002$	$0.051 \pm 0.002$
GBM	Band	—	—	$1.51 \pm 0.16$	$70 \pm 17$	$2.5 \pm 0.7$	564 / 436	$0.023 \pm 0.036$	$0.032 \pm 0.049$
XRT-BAT-GBM	db-pl	$1.14 \pm 0.03$	—	$1.81 \pm 0.05$	$132^{+49}_{-16}$	—	643 / 674	—	—

In the case of GBM data we provide here the photon index for a single power-law SED (s-pl) and a Band function (Band et al. 1993), with the corresponding peak energies in units of keV. The last two columns give the photon flux  $F_{\text{ph}}$  [ph/cm<sup>2</sup>/s] in the high-energy domain from 0.3 to 1 MeV and 0.3 to 10 MeV, respectively, extrapolated from the GBM data. BAT/GBM combines BAT and GBM data, XRT-BAT-GBM further uses the XRT data. In these cases the fit was performed using a double broken power-law (db-pl), with the corresponding break energies in units of keV. Note that in our notation the  $\tilde{\beta}$  is the photon index and the observed photon flux is proportional to  $E^{-\tilde{\beta}}$ . In case of combined BAT/GBM fits,  $\tilde{\beta}_3$  was always ill-defined.

During our first two epochs of GROND observations (Rossi et al. 2008a) the weather conditions were not good, with the seeing always higher than 2''5 and strong winds (> 10 m/s). Therefore, it was not possible to separate the afterglow from a nearby galaxy that first became separately visible on the 3rd epoch images (seeing 1''5; see Sect. 3.4). In order to correct for the contribution of this galaxy, we performed image subtraction using the HOTPANTS package<sup>7</sup>. We applied image subtraction on the first, second and third epoch GROND images, using the fifth GROND epoch images as a template. This gave good results for all bands except  $g'$ , which is affected by a low-quality point spread function. Therefore, for this band we performed a simple subtraction of the flux of the galaxy component, with the flux derived from the 5th epoch images. The local secondary standard stars used to calibrate the field are listed in Table A.4.

Watcher data (Ferrero et al. 2008), VLT data (Vreeswijk et al. 2008; Fynbo et al. 2009), and ROTSE-IIIa data were calibrated using USNO-B1 field stars. In order to take these different calibrations into account, we compared the  $r'$ -band photometry of the GROND secondary standard stars with the corresponding  $R$ -band magnitudes from USNO-B1. In doing so, we obtained a correction of  $0.40 \pm 0.15$  mag for USNO-B1. After shifting these afterglow data to the GROND  $r'$  band, we finally subtracted the GROND 5th epoch flux of the galaxy closest to the afterglow (see Sect. 3.4) from the Watcher and VLT observed magnitudes, which shifted the afterglow magnitude by +0.05 mag and +0.11 mag, respectively. The correction for the ROTSE-IIIa data was even smaller and, therefore, set to zero. The complete data set is shown in Fig. A.1.

### 3. Results and Discussion

#### 3.1. The prompt emission phase

##### 3.1.1. From gamma-rays to X-rays

The prompt gamma-ray emission is dominated by a strong peak starting at 170 s, which reached its maximum at 204 s and was

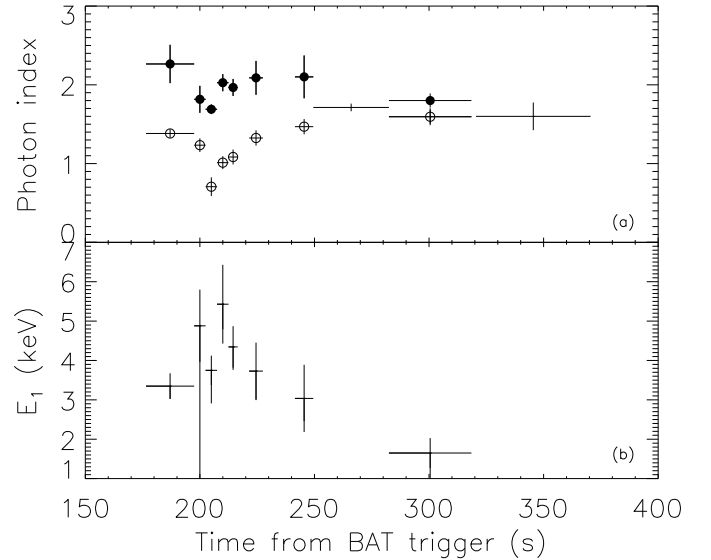


**Fig. 3.** Spectral parameters of the prompt emission using the time-resolved XRT-BAT-GBM data. (a): The evolution of the photon index from fits to BAT-GBM and XRT data. Open circles show the low-energy index  $\tilde{\beta}_1$  below the break energy  $E_1$  of a single broken power-law and the filled circles represent the high-energy index  $\tilde{\beta}_2$  above  $E_1$ . Points with no plot symbols (error bars only) are the best-fit results using a simple power-law only. (b): The low-energy break energy,  $E_1$ , from fits to the BAT and XRT data. During the flare at 208 s spectral evolution is seen, similar to what was also detected in other afterglows (e.g., Falcone et al. 2007).

detected by GBM and BAT and also seen by XRT. In addition, XRT also detected a second weaker peak at 357 s. The first peak was also detected by UVOT in the white band.

During the first peak of the prompt emission (in the interval  $t_0 - 23.5 \text{ s} < t < t_0 + 16.5 \text{ s}$ ) we could fit only a simple power-law to the BAT data with a photon index  $1.67 \pm 0.34$ . We also fitted the BAT-GBM data during the second peak ( $t_0 + 46.5 \text{ s} < t < t_0 + 121 \text{ s}$ ) and the XRT-BAT-GBM data during the main peak

<sup>7</sup> <http://www.astro.washington.edu/users/becker/hotpants.html>

( $t_0 + 198.75 \text{ s} < t < t_0 + 228.4 \text{ s}$ ). For both peaks we found a peak energy of  $\approx 130 \text{ keV}$ , though we could not constrain the index above the peak (Table 1). No spectral analysis was possible for the precursor.

For the GBM-only data, two different empirical models were applied to fit the spectra: a simple power-law and a Band function (Band et al. 1993), which smoothly connects two power-laws. The burst was faint for the GBM, especially at energies above  $150 \text{ keV}$ . Thus, the more complex model of a Band function could not be constrained sufficiently and the simple power-law is preferred for both time intervals.

Table 1 summarizes the fits of the SED for the XRT-BAT-GBM data for two time intervals around the main peak in the gamma-ray light curve. In particular, we performed a spectral fit for the peak centered around  $204 \text{ s}$ . For joint fits with BAT and XRT, we used an absorbed power-law with the Galactic and the GRB host column densities fixed to the values found in Sect 2.2.

Figure 3 shows the time evolution of the SED in the BAT band and the joint BAT-XRT band during the first  $400 \text{ s}$  after the BAT trigger. For the three early peaks in the BAT light curve (Fig. 1) the error bars are too large to indicate any spectral evolution. During the main gamma-ray peak at  $204 \text{ s}$ , however, there is evidence for a spectral softening when the peak is developing and a spectral hardening after the peak. After the light curve peak, the situation is reversed. This behaviour is similar to what has been found for GRB 060714 (Krimm et al. 2007). Also, the power-law indices as well as the break energy are consistent with the corresponding values found in gamma-ray flares (Krimm et al. 2007).

In the cases where a broken power-law model is the best fit ( $\Delta\chi^2 > 4$ ) the break energy as well as the high-energy index and the low-energy index are well constrained. So, essentially BAT is fitting the high-energy index, XRT is fitting the low-energy index and the joint fit fits an average index, becoming dominated by the low-energy emission where the BAT statistics are poor. Remarkably, even though the break energy is always between  $1$  and  $5 \text{ keV}$ , i.e. well below the BAT and GBM window, the prompt emission flare is still very bright in BAT and GBM. Moreover, it is  $10$  times brighter than the peak on which BAT triggered.

### 3.1.2. From gamma-rays to the optical

GRB 080928 is one of those exceptional cases where optical and X-ray data could be obtained while the source was still being detected in the gamma-ray band (Fig. 4). The analysis of the joint UVOT-XRT-BAT-GBM SED allows us to follow the evolution of the prompt emission during all the main flaring activity observed between  $199$  and  $557$  seconds after the trigger from  $1 \text{ eV}$  to  $150 \text{ keV}$ .

The prompt gamma-ray emission detected by BAT and GBM is dominated by the strong peak at  $204 \text{ s}$ . Possibly physically related to that is a strong peak in the X-ray emission seen by XRT about  $4$  seconds later at  $208 \text{ s}$ , which was followed by a less intense X-ray peak at  $357 \text{ s}$ . The latter has no obvious counterpart in the gamma-ray emission. The optical light curve monitored by UVOT shows a first peak at  $(249 \pm 10) \text{ s}$ , i.e.  $45$  seconds after the main peak of the prompt emission and  $41 \text{ s}$  after the main peak in the X-ray flux.

In order to gain deeper insight into the early emission properties and on their time evolution, we now included the optical data and constructed the SED from the optical to the gamma-ray band for six time intervals defined by the first six optical detections by UVOT, starting at  $199 \text{ s}$  and finishing  $479 \text{ s}$  after the

trigger (Table 2, Fig. 4). In doing so, we exclude the 6th optical measurement (ROTSE-IIIa) because it covers a rather big time interval.

During the first five time intervals BAT as well as GBM were still detecting gamma-ray emission (the main gamma-ray peak occurred when UVOT was already observing), while during the last two time intervals the fluence in the gamma-ray band was too low to constrain the spectral properties. Figure 5 shows the fit to the data from about  $1 \text{ eV}$  to up to  $150 \text{ keV}$ . In the following, we first focus on SED #1. Here, we fit the data with a broken power-law with the X-ray data corrected for Galactic and GRB host absorption (see Sect. 3.2.1) and the optical data corrected for the Galactic and GRB host extinction.

For the time interval #1 (Table 2) we have combined the first optical UVOT detection (Table A.2) with the XRT and the BAT-GBM detection from  $202.8 \text{ s}$  to  $206.9 \text{ s}$ . A sharp break is clearly visible at an energy around  $5 \text{ keV}$  (in case of SED #1 the soft X-ray data,  $E < 1 \text{ keV}$ , shows too much scatter and therefore could not be used for the analysis). Assuming that SED #1 represents the spectral energy distribution of synchrotron light of a single radiating component from about  $1 \text{ eV}$  to  $150 \text{ keV}$  (see also Shen & Zhang 2009), we fitted the data with a broken power-law while fixing the low-energy index to its theoretically expected value  $\beta = -1/3$  (i.e., rising with energy). The slope of the high-energy index is then found to be  $\beta = 0.72 \pm 0.06$  ( $\chi^2/\text{d.o.f.} = 66.8/75$ ) with a spectral break at an energy of  $4.30 \pm 0.45 \text{ keV}$ . The corresponding UVOT data point lies  $1\sigma$  below the best fit (Fig. 5).

If we identify the break in the SED as the position of the minimum injection frequency  $\nu_m$  of an ensemble of relativistic electrons in the slow cooling regime ( $\nu_m < \nu_c$ , with  $\nu_c$  being the cooling frequency), then we expect a low-energy spectral index of  $-1/3$  and a high-energy spectral index of  $(p - 1)/2$ , where  $p$  is the power-law index of the electron distribution function ( $N(\gamma)d\gamma \propto \gamma^{-p}d\gamma$ ). The measured low-energy spectral index ( $-0.39 \pm 0.06$ ) is basically in agreement with the theoretically expected value. The measured high-energy spectral index is  $0.72 \pm 0.06$ , leading to  $p = 2.44 \pm 0.12$ , which is a reasonable value for relativistic shocks, both theoretically (Achterberg et al. 2001; Kirk et al. 2000) as well as observationally (e.g., Kann et al. 2006; Starling et al. 2008; Curran et al. 2010).

On the other hand, if the break is the cooling frequency in the fast cooling regime, then we expect a low-energy spectral index of  $-1/3$  and a high-energy spectral index of  $0.5$ . Within errors the latter disagrees with the observations, the spectral slope is  $0.72 \pm 0.06$  and the discrepancy is  $3.7\sigma$ . However, it is quite possible that the snapshot of the high-energy part of the SED we observe in our time window is the average of a rapidly evolving SED that accompanied the rapidly evolving light curve.

Making the step to the SEDs #2 to #4, we are faced with the problem that the break seen in SED #1 is not detectable anymore, most likely because the peak energy  $E_p$  has moved to lower energies. However, given that we see a large flare in the X-ray light curve, part of the data do allow us to investigate if the evolution of the SED is compatible with large-angle emission.

### 3.1.3. Large-angle emission

X-ray flares are commonly observed in GRB afterglows, with the most prominent example being GRB 050502B (e.g., Chincarini et al. 2007, 2010; Burrows et al. 2005b). The early flares of GRB 080928 are among the strongest flares seen so far. While much stronger flares have been observed (GRBs 060124,

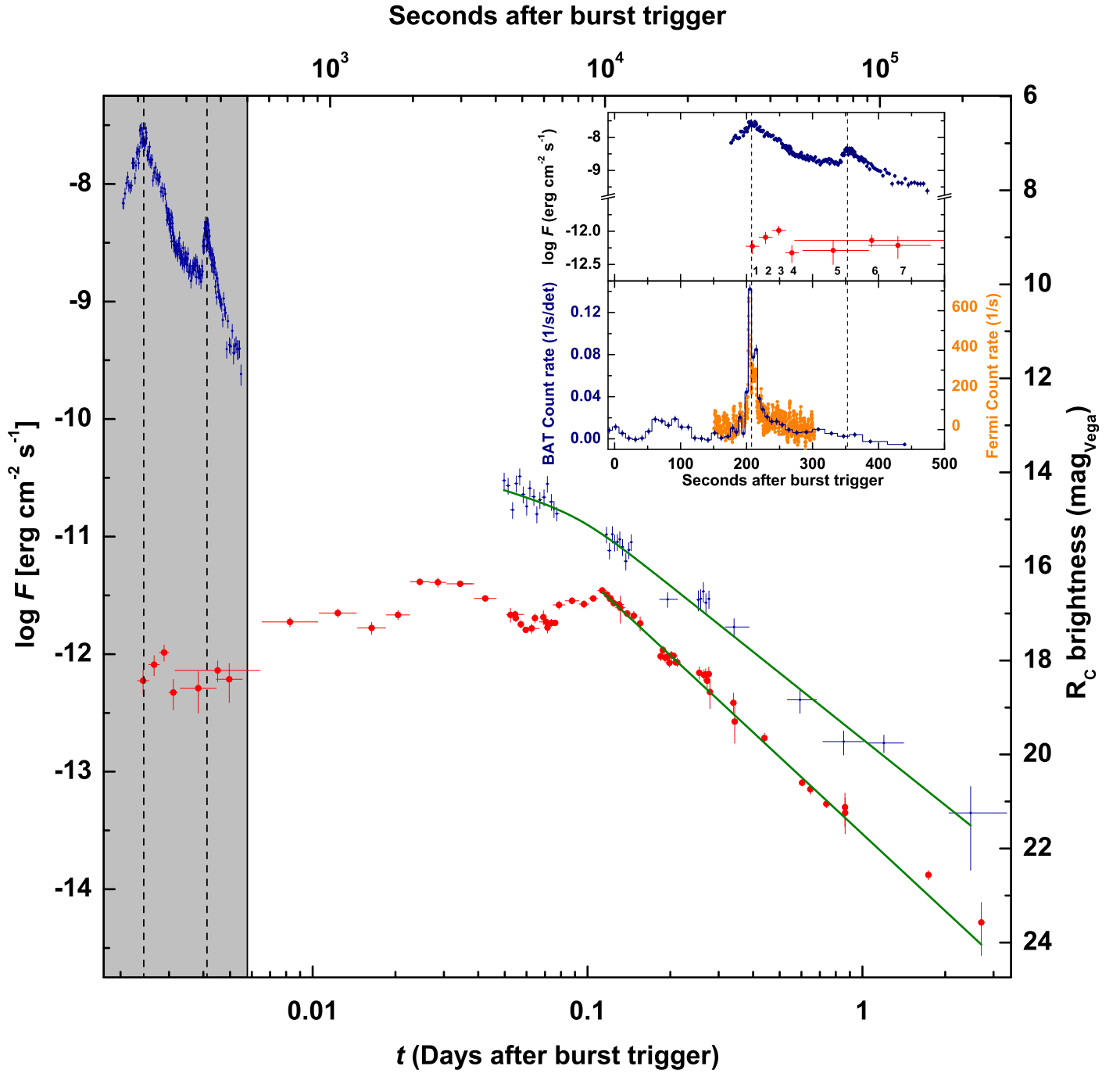


**Fig. 4.** Temporal evolution of the optical (composite light curve with all data shifted to the  $R_c$  band) and X-ray afterglow (0.3 to 10 keV) of GRB 080928 (optical: red circles, X-ray: blue error bars). The upper limits are not shown here to avoid confusion. The zoom-in shows the early phase (also highlighted in gray in the big figure) where it is compared with the BAT-GBM prompt emission. The dashed vertical lines indicate the peak times of the two X-ray flares. The curve represents the best fit of the late-time data.

Romano et al. 2006; 061121, Page et al. 2007), the first flare seen in the afterglow of GRB 080928 is even stronger in terms of peak count rate than the flare of GRB 050502B. In particular, it has good enough data to investigate if its radiation tail can be interpreted as large-angle emission (LAE; Fenimore & Sumner 1997; Kumar & Panaitescu 2000).

Figure 4 shows that between epoch #3 and #4 the optical light curve is falling, while thereafter it remains constant (within errors). The figure also shows that after the 5th optical epoch the X-ray light curve has a 2nd flare. This makes it likely that

the nature of the main emission component changed after the 3rd time interval. Having this in mind, we included only the first three data points in Table 2 in our analysis. In doing so, we fixed the value for the spectral slopes to the one for SED #1 ( $\beta = -1/3$  for the low-energy part as given by synchrotron theory and 0.72 for the high-energy part as it follows from the fit).

Within the standard LAE model, there is a one-to-one correspondence between photon arrival time  $t$  and location of emitting fluid:  $t = (1 + z)r\theta^2/c$ , where  $r$  is the source radius and  $\theta$  the direction of fluid motion relative to the center-observer line.

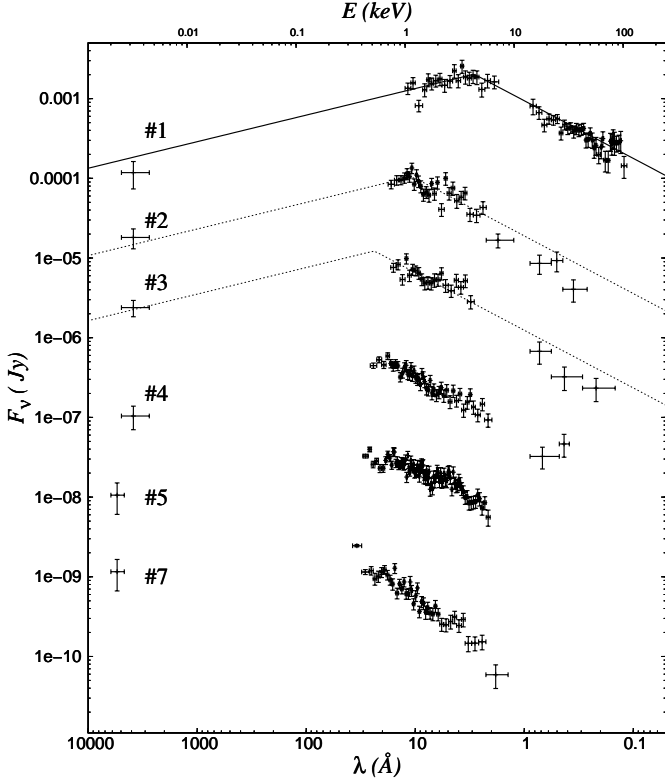


**Fig. 5.** The spectral energy distribution of the combined early emission during the time when the first six optical data points were obtained by *Swift*/UVOT *white* and *v* filters. The corresponding time intervals are listed in Table 2. The fluxes of the curves #2, 3, 4, 5, and 7 have been multiplied for clarity by  $10^{-1}$ ,  $10^{-2}$ ,  $10^{-3}$ ,  $10^{-4}$ , and  $10^{-5}$ , respectively. The fits for #2, 3 were obtained by fixing the high-energy slope to the corresponding slope obtained for SED #1, the low-energy slope to  $1/3$ , and by matching the expected break energy following the non-standard LAE model (Sec. 3.1.3).

So, the observer receives emission from fluid regions moving at progressively larger angles  $\theta$ . Thus, at different times, the observer receives emission from different regions and from different electrons. Thereby, the following assumptions are made: (1) the electron population is the same at all angles  $\theta$  and (2) the surface brightness of the emitting shell is uniform in angle. From these assumptions, it follows that the flux decreases as  $t^{-(2+\beta)}$ . From the first assumption, it follows that the peak energy should decrease as  $t^{-1}$ . In the  $\nu^{1/3}$  part of the spectrum, the optical LAE should then decay as  $t^{-5/3}$ . However, our data show that the optical flux is rising between epoch 1 and 3 (Fig. 4).

If the entire emission between the 1st and the 2nd X-ray flare is of LAE origin, then the fact that the optical flux increases at epochs 2 and 3 (instead of decreasing as  $t^{-5/3}$ ), while the X-ray flux decreases implies that the aforementioned assumption (1) of the LAE model is incorrect. In particular, it implies that  $E_p$  for the electrons at larger angles (corresponding to epoch 3) is lower than at smaller angles (corresponding to epoch 1), at the same lab-frame time. In other words, the rising optical flux is compatible with the LAE interpretation only if  $E_p$  decreases with observer time faster than  $t^{-1}$ .

Therefore, we applied a non-standard LAE model. We assumed that the local synchrotron peak flux  $F_p$  as well as the peak energy  $E_p$  depend on the viewing angle  $\theta$ . In doing so, we make the ansatz that an observer located at an angle  $\theta$  relative

**Table 2.** Results of the joint optical to gamma-ray spectral fit ( $\sim 1$  eV to  $\sim 150$  keV).

#	Optical time	Optical interval	XRT-BAT-GBM time	XRT-BAT-GBM interval	$E_{\text{break}}$ (keV)
1	208.7	199.0 - 219.0	204.8	202.8 - 206.9	4.30(45)
2	228.7	219.0 - 238.0	231.0	227.5 - 234.5	1.16(48)
3	248.7	239.0 - 258.0	245.5	241.5 - 249.5	0.52(27)
4	268.7	259.0 - 278.7	268.7	259.0 - 278.7	–
5	331.3	285.0 - 385.0	344.4	318.5 - 372.5	–
6	389.6	272.7 - 556.7	361.0	272.7 - 477.9	–
7	429.3	385.0 - 478.7	428.9	385.0 - 477.9	–

Here we show seven time intervals (given in units of seconds) defined by the first seven optical data points (Fig. 4) during the early emission component of GRB 080928 (Fig. 5). The 6th optical measurement (ROTSE-IIIa) covers a rather big time interval, therefore we did not use it for the study of the time evolution of the break energy. The 2nd and the 4th column give the logarithmic mean time. The last column gives the break energy including its error, computed inside the non-standard LAE model predictions, for epochs 1 to 3 assuming  $t_p = 185.9$  s. For further details see Sect. 3.1.2.

to us would observe a peak flux and peak energy evolving as  $F_p(\theta) \propto \theta^{-2a}$  and  $E_p \propto \theta^{-2b}$ , respectively. The evolution of the measured peak flux and peak energy after relativistic boosting is then  $F_p \propto (t-t_p)^{-2-a}$  and  $E_p \propto (t-t_p)^{-1-b}$ , respectively, where  $t_p$  is the unknown zero-point. The resulting LAE X-ray light-curve above the peak energy  $E_p$  in the  $\nu^{-\beta}$  part of the SED is then

$$F_x \propto (t - t_p)^{-2-\beta-a-b\beta}, \quad (2)$$

while the LAE optical light-curve (below the peak energy, in the  $\nu^{1/3}$  part of the SED) is described by

$$F_{\text{opt}} \propto (t - t_p)^{-5/3-a+b/3}. \quad (3)$$

In order to check this model, we fixed the peak energy to  $E_p = 4.3$  keV at epoch 1 and the spectral slope to  $\beta = 0.72$  (Table 2). We fitted the X-ray and optical data between 205 and 250 s after the trigger, i.e., between epochs 1 and 3, when the optical light curve was rising. This gives  $t_p = (185.9 \pm 7.5)$  s,  $a = -1.2 \pm 0.2$ , and  $b = 1.1 \pm 0.5$ , where the latter parameters follow via Eq. 3 from the derived decay slopes. Figure 5 shows how the fit is able to follow the SED during epochs #2 and #3. The fit puts the time zero-point at the beginning of the main emission of the proper GRB. This finding is qualitatively in line with other studies of other X-ray afterglows (e.g. Liang et al. 2006).

While the fit is satisfactory, one might wonder why at epoch 1 the low-energy part of the SED touches the optical data point only within  $1\sigma$ . However, there is actually much more uncertainty in the extinction-corrected UVOT flux than it is simply given by the measurement error of 0.25 mag (*white* filter; Roming et al. 2009 see Table A.2). The biggest uncertainty<sup>8</sup> comes from the correction for extinction in the GRB host galaxy. Assuming a Milky Way extinction law, a ratio of total-to-selective extinction of  $R_V = 3.08$  (i.e. the standard value), and  $A_V^{\text{host}} = 0.12$  mag (Table 4) gives a correction for host extinction in the UVOT *white* filter of 0.52 mag (including the cosmological  $k$ -correction and the correct CCD sensitivity characteristics in case of UVOT/white filter observations<sup>9</sup>). However,  $R_V$  in

<sup>8</sup> A smaller uncertainty comes from the Galactic reddening derived from Schlegel et al. (1998), which percentage error can be large for low reddening values.

<sup>9</sup> <http://heasarc.gsfc.nasa.gov/docs/heasarc/caldb/data/swift/uvota/>

the star-forming region where the GRB went off is not exactly known. Its  $1\sigma$  error might well be in the order of 50%. Finally, the host extinction we have derived here (Table 4) is based on data taken 20 ks after the burst. It is an open question if the host extinction was the same amount already 200 s after the onset of the burst. In other words, the fact the UVOT white filter measurement does not exactly correspond to the low-energy SED extrapolated from the X-ray data should not be overinterpreted. However, it naturally affects our test of the LAE model since it introduces additional uncertainties.

### 3.2. The afterglow phase

#### 3.2.1. The light curve

At early times, up to 470 s after the trigger, the X-ray light curve is dominated by two strong peaks (Fig. 4). The first peak is 4 seconds after the peak seen by BAT and GBM. The optical light curve is similarly complex, showing bumps up to about 10 ks after the trigger. Unfortunately, the gap in the X-ray data does not allow for a comparison between the two bands during this timespan.

Despite the rich variability in the early afterglow, the late time evolution is consistent with a power-law decay. After 4.2 ks the X-ray light curve can be described by a broken power-law (Beuermann et al. 1999) with  $\alpha_1^X = 0.72 \pm 0.35$ ,  $\alpha_2^X = 1.87 \pm 0.07$ ,  $t_b = (8100 \pm 1600)\text{s}$  (observer frame), and a fixed smoothness parameter  $n = 5$  ( $\chi^2/\text{d.o.f.} = 55.4/33 = 1.68$ ; Fig. 4). The optical data do not allow for a fit with a broken power-law. For  $t_{\text{obs}} > 10$  ks the fit with a single power-law gives  $\alpha^{\text{opt}} = 2.17 \pm 0.02$  ( $\chi^2/\text{d.o.f.} = 56.8/34 = 1.67$ ). The optical/NIR and X-ray data suggest similar small variability after 20 ks, which however we cannot study further due to the sparsity of the data. The break in the X-ray light curve could be a jet break, but as we will argue later, our detailed modeling of the afterglow does not support this conclusion (Sect. 3.2.3).

In Fig. 6 we compare the X-ray afterglow of GRB 080928 with all X-ray afterglows found up to April 2010 in a redshift interval of  $\Delta z = 0.1$  around the redshift of GRB 080928 (1.6919), namely GRB 050802 ( $z = 1.7102$ ; Fynbo et al. 2009), 071003 ( $z = 1.60435$ ; Perley et al. 2008b), 080603A ( $z = 1.6880$ ; Perley et al. 2008a), 080605 ( $z = 1.6403$ ; Fynbo et al. 2009), 090418 ( $z = 1.608$ ; Chornock et al. 2009), 091020 ( $z = 1.71$ ; Xu et al. 2009), and 100425A ( $z = 1.755$ ; Goldoni et al. 2010). In comparison to these, the early X-ray emission of GRB 080928 is about 1.6 dex more luminous, probably due to its physical connection to the prompt emission. Even compared to the entire ensemble of 190 X-ray light curves, it is more luminous than the average. However, after the light curve break at 8.1 ks (observer frame; 3 ks host frame) the afterglow rapidly becomes sub-luminous with respect to the ensemble. Interestingly, except for GRB 080603A and 100425A, the other afterglows have a similar break time and post-break decay slope.

In the optical bands the afterglow tends to vary between two extremes. We correct the afterglow for the extinction derived below (Sect. 3.2.2) and shift it to  $z = 1$  following Kann et al. (2006). Compared to the ensemble of optical afterglows with reasonable data (Kann et al. 2010), at early times it is comparatively faint, nearly eight magnitudes fainter than the brightest events (Fig. 7). Its multiple rebrightenings, which are a notable signature of this afterglow, then bring the late-time light curve close to the mean magnitude of the distribution at one day after the GRB (at  $z = 1$ ). In between, at about 0.1 days (at  $z=1$ ), they make the afterglow about 2 mags brighter than the average, shift-

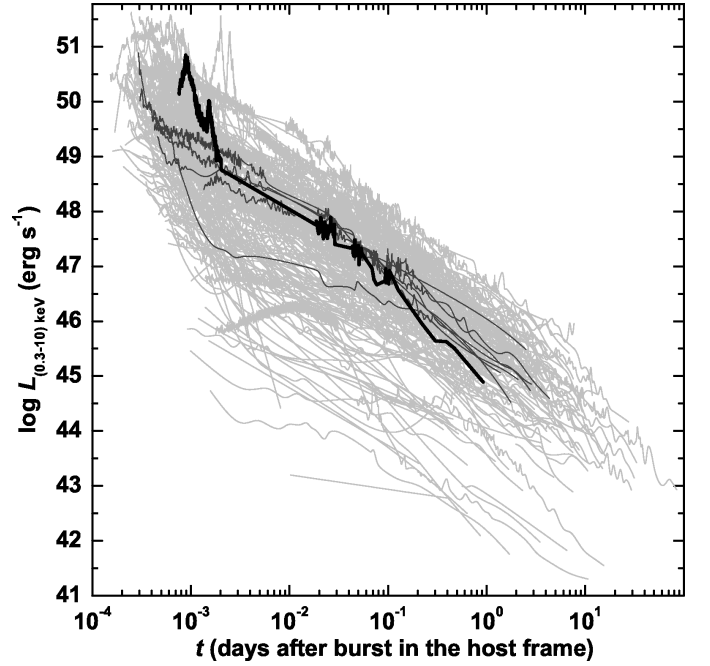


**Fig. 6.** The X-ray luminosity of 190 *Swift* GRBs and their afterglows in the range of 0.3 to 10 keV between Jan 26, 2005, and Apr 25, 2010. GRB 080928 is shown in black. For comparison all six GRBs within a redshift interval of 0.1 around the redshift of GRB 080928 are highlighted in dark gray. The luminosity of the afterglow of GRB 080928 was basically in the mean of the X-ray luminosities which have so far been observed.

ing it into the group of the 10 top brightest optical afterglows at that time.

#### 3.2.2. The broad-band SED

In order to fit the unabsorbed SED from the optical to the X-ray band we selected the X-ray data from 12.4 ks to 25 ks (mean photon arrival time 20 ks). Since no evidence for color variations was found in the optical data, we then shifted the optical light curve to this time (Table 3; corrected for a Galactic extinction of  $E(B - V) = 0.07$  mag). In addition to the GROND and UVOT data we used the VLT detection corrected to the  $R_C$  band (Sect. 2.3). In doing the fit, we fixed the redshift to 1.69, the host galaxy hydrogen column density to  $N_H = 3.5 \times 10^{21} \text{ cm}^{-2}$  and the Galactic hydrogen column density to  $N_H = 0.56 \times 10^{21} \text{ cm}^{-2}$  (Sect. 2.2). The resulting SED is shown in Fig. 8 (left) and Table 4. There is no spectral break between the X-ray band and the optical. Between 4 ks until the end of the X-ray observations at around 120 ks (1.4 days) no evidence for spectral evolution was found.

We find that SMC and LMC dust provided an acceptable fit, although MW dust improved the fit (Table 4). The  $2175\text{\AA}$  feature is less strong than in the case of GRB 070802 (Krühler et al. 2008; Elíasdóttir et al. 2009), however. The derived host extinction is clearly unremarkable within the sample of Kann et al. (2010).

For a Milky Way interstellar medium the deduced high  $N_H$  would imply a host extinction of  $A_V^{\text{host}} = 2_{-1.2}^{+1.0}$  mag, in contrast to the small value found here. However, several GRB afterglows studies have found that, despite a very large scatter in the  $N_H/A_V$  ratio, the  $N_H$  is always significantly larger than that observed in the local Universe (e.g., Galama & Wijers 2001; Stratta et al.



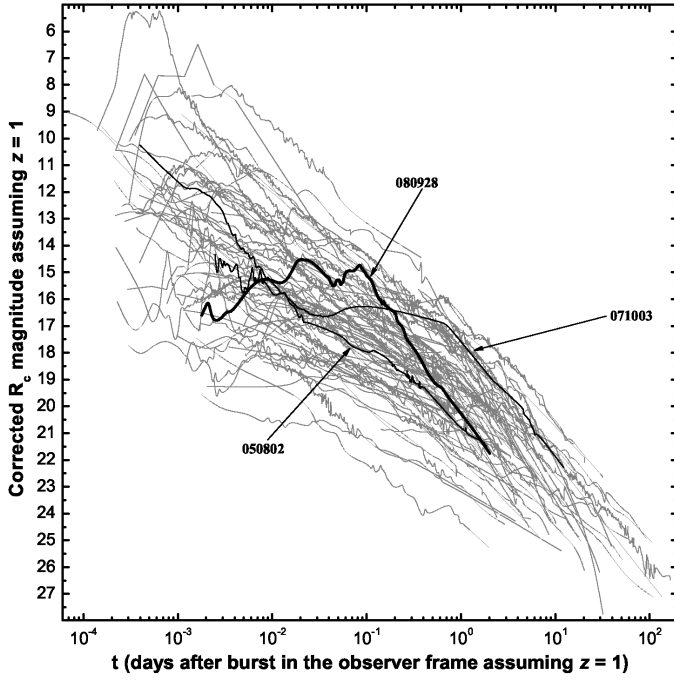


**Fig. 7.** The optical afterglow of GRB 080928 (thick line) compared with the sample of extinction-corrected afterglows shifted to  $z = 1$  from Kann et al. (2010). For comparison, the GRBs within a redshift interval of 0.1 around the redshift of GRB 080928 for which we have optical data are highlighted and labelled. All magnitudes are Vega magnitudes.

**Table 3.** The values plotted in Fig. 8.

Filter	$\lambda$ (nm)	$\nu(1+z)$ ( $10^{14}$ Hz)	mag	$F_\nu$ ( $\mu$ Jy)
$K_S$	2151.2	3.75	$15.07 \pm 0.13$	$653.8 \pm 102.4$
$H$	1646.7	4.90	$15.86 \pm 0.12$	$460.7 \pm 52.7$
$J$	1256.1	6.42	$16.66 \pm 0.09$	$340.0 \pm 26.6$
$z'$	893.0	9.04	$17.56 \pm 0.06$	$213.4 \pm 11.4$
$i'$	762.6	10.58	$17.84 \pm 0.05$	$186.2 \pm 9.29$
$R_C$	658.8	12.25	$18.36 \pm 0.15$	$140.0 \pm 19.4$
$r'$	627.0	12.87	$18.47 \pm 0.05$	$129.6 \pm 6.05$
$v$	550.5	14.66	$18.71 \pm 0.10$	$119.4 \pm 11.0$
$g'$	455.2	17.73	$18.91 \pm 0.10$	$97.8 \pm 9.07$
$b$	444.8	18.14	$18.90 \pm 0.08$	$111.7 \pm 8.64$
$u$	365.2	22.10	$18.48 \pm 0.04$	$73.7 \pm 2.81$
$uvw1$	263.4	30.64	$18.92 \pm 0.11$	$23.8 \pm 2.38$
$uvm2$	223.1	36.17	$20.53 \pm 0.30$	$5.40 \pm 1.51$
$uvw2$	203.0	39.76	$> 19.81$	$< 11.4$

The data refer to  $t = 20$  ks. Data are corrected for Galactic extinction and are given in Vega magnitudes. The  $R_C$ -band value is based on Vreeswijk et al. (2008); the other data refer to the GROND and the UVOT filter bands.

2004; Kann et al. 2006; Starling et al. 2007; Schady et al. 2007, 2010), a phenomenon that potentially could be explained by dust destruction by the intense fireball light (Fruchter et al. 2001; Watson et al. 2007).

### 3.2.3. Theoretical modeling of the light curve

Using the forward shock afterglow model (e.g., Panaitescu & Kumar 2000; Zhang & Mészáros 2004; Piran

**Table 4.** Results of the joint optical to X-ray spectral fit.

Dust model	$A_V^{\text{host}}$	$\beta_{\text{OX}}$	$\chi^2/\text{d.o.f}$
MW	$0.12 \pm 0.03$	$1.03 \pm 0.01$	20.2/18
LMC	$0.07 \pm 0.02$	$1.02 \pm 0.01$	24.5/18
SMC	$0.04 \pm 0.01$	$1.01 \pm 0.01$	26.6/18

The first column gives the dust model, the following columns the deduced host extinction, the spectral slope from the optical to the X-ray band and the  $\chi^2$  with the corresponding degrees of freedom.

2005), it is difficult to explain the different slopes of the optical and X-ray light curves given that they are on the same power-law segment of the spectrum. Assuming the cooling frequency,  $\nu_c$ , is above the X-ray band, the spectral slope gives an electron energy index of  $p = 2\beta + 1 \approx 3$ . The light curve slope of  $\alpha \approx 2$  then indicates we have a pre-break evolution in a stellar wind. This would be problematic for the early-time evolution, as it is difficult to get a rising afterglow with a stellar wind external medium. The second possibility is that  $\nu_c$  is below the optical band, resulting in  $p = 2\beta \approx 2$ . The light curve slope then indicates we are in a post-break evolution. If the external medium is constant we are not in contradiction with the early time observations, given a small enough initial Lorentz factor. Having  $\nu_c$  below the optical band is, however, difficult to achieve as we will show below.

The early optical light curve is rich in variability. Unfortunately, there are no XRT measurements during the optical fluctuations to verify the correlation between X-ray and optical light curves, but there are a couple of other cases where high-energy flares are seen in the optical too, e.g., GRB 041219A (Vestrand et al. 2005; Blake et al. 2005), GRB 050820A (Vestrand et al. 2006), GRB 060526 (Thöne et al. 2010), GRB 061121 (Page et al. 2007) and XRF 071031 (Krühler et al. 2009). In particular, the general behaviour of the afterglow recalls the cases of GRB 060904B (Klotz et al. 2008; Kann et al. 2010) and GRB 060906 (Cenko et al. 2009). The optical fluctuations have a long timescale which is more consistent with energy injection into the forward shock than with central engine activity.

We used the numerical model of Jóhannesson et al. (2006) and Jóhannesson (2006), with modifications as described in Pérez-Ramírez et al. (2010), to fit the afterglow data. We excluded data taken in the first 500 s after the trigger, as they are most likely explained by internal shocks. The data are still kept in the fit as upper limits: not accounted if the model is below, but added to the  $\chi^2$  value like normal points if the model is above. We explored two different times as the initial time for the calculation: the trigger time  $t_0$  and the start of the main prompt emission at  $t_0 + 170$  s. Since a wind-like medium will over-predict the early data, we limited our study to a constant-density medium. Our assumption was that the first peak in the optical light curve at  $\sim 1000$  s is the onset of the afterglow and the following two bumps at  $\sim 2$  ks and  $\sim 10$  ks are caused by energy injections. Host extinction was assumed to be Milky-Way like as found from the spectral analysis but we allowed  $A_V^{\text{host}}$  to be free during the fit. We accounted for Ly  $\alpha$  extinction with the method of Madau (1995).

In the forward shock model it is generally assumed that the shock front expands sideways at the speed of sound. Using numerical calculations, Kumar & Granot (2003) found that the expansion speed of the jet is significantly lower than this simple estimate. One of the effects of a slower sideways expansion is

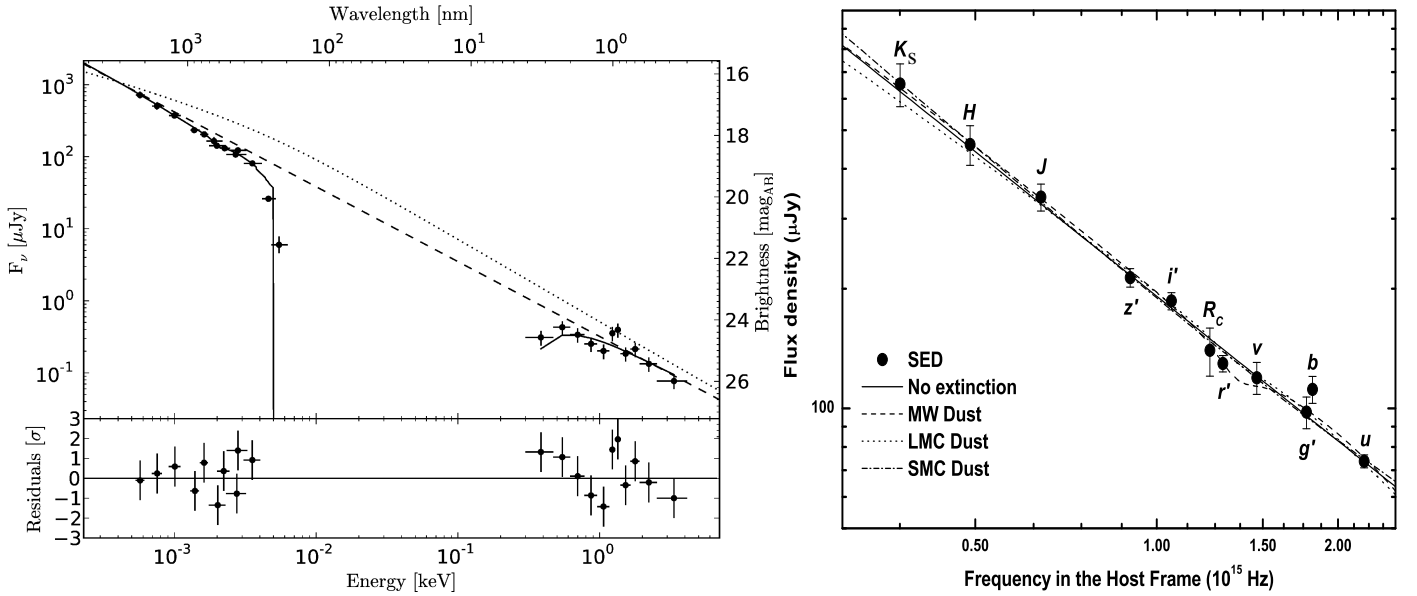


**Fig. 8.** The observed SED of the X-ray/optical/NIR afterglow of GRB 080928 at  $t=20$  ks after correction for Galactic extinction by dust and Galactic absorption by gas. *Left:* The joint X-ray/optical SED is almost a pure power-law (dashed line) affected by only a small amount of host extinction by dust (Table 4) and  $3.5 \times 10^{21} \text{ cm}^{-2}$  of host absorption by the gas. The UV bands are affected by Lyman drop-out. The dotted line represents the SED that follows from the numerical energy injection model for this particular time, which slightly overpredicts the flux in the X-ray band (see Sect. 3.2.3). Residuals refer to the plot with  $\beta_{\text{OX}} = 1.02$  (broken line). *Right:* Zoom-in into the optical/NIR SED, and the different dust models used to fit the data, where it is possible to discern the dip resulting from the 2175 Å feature.

that the jet break is reached later in the evolution. This poses some problems when fitting the sharp overturn after the last optical bump as the energy injections effectively move the evolution of the forward shock back in time. We have found that reducing the expansion speed to  $\sim 20\%$  of the speed of sound mitigates this problem, in agreement with the values found by Kumar & Granot (2003). We note that this is an upper limit on the expansion speed, lower values can be used to explain the data.

Table 5 gives the parameters of the best fit model shown in Fig. 9. The numerical model prefers the start time of  $t_0 + 170$  s where most of the constraints come from the optical data contemporaneous with the high-energy prompt emission. The model over-predicts the data in this epoch when the start time is  $t_0$ . The best fit results in  $\chi^2/\text{d.o.f.} = 307/187 = 1.64$ , which is comparable to the power-law fits shown earlier despite fitting more data. We note that the fit does not do a good job with the X-ray light curve, slightly under-predicting it before the second injection and then over-predicting it afterwards. This seems to indicate that there is some other mechanism at work than energy injections, but the lack of simultaneous X-ray observations during the optical rise makes it difficult to say what is going on.

Unfortunately, we are unable to find a suitable set of initial parameters such that we have  $\nu_c$  below the optical frequency and do not over-predict the flux. This is caused by the fact that in post-break evolution we have (Rhoads 1999)

$$\nu_c \propto \epsilon_B^{-3/2} n_0^{-5/6} E_0^{-2/3}, \quad (4)$$

$$F_{\text{max}} \propto \epsilon_B^{1/2} n_0^{1/6} E_0^{4/3}, \quad (5)$$

where  $F_{\text{max}}$  is the afterglow flux at the peak frequency,  $\epsilon_B$  is the fraction of energy contained in the magnetic field,  $n_0$  is the density of the external medium, and  $E_0$  is the initial energy release. As we see from these equations, it is very difficult to lower the value of  $\nu_c$  without increasing the flux of the afterglow. This can

be overcome by placing the break frequency close to the optical waveband and increasing the absorption. The spectrum from the numerical fit is shown in Fig. 8 and it explains the data equally well as a single power-law. One must also note that the cooling break is not sharp as we are integrating over the equal arrival time surface with different intrinsic values for the cooling break.

The error estimates given in Table 5 are found from a  $\chi^2$  profile method and we consider these errors to be reliable. Due to lack of radio and mm data, our limit on  $n_0$  is mostly from the requirement for an early jet-break although the low value of  $\nu_c$  also plays a role. The limit on the initial Lorentz factor,  $\Gamma_0$ , is found from the requirement that the first optical bump coincides with the onset of the afterglow. The low value of  $\Gamma_0 \sim 100$  favours a high-energy spectral slope of 2.5 as it is indicated by the Band function fit in Table 1.

The initial half opening angle of the jet,  $\Theta_0$ , has an unusually low value, required by the assumed small jet break time of 10 ks. This low value is also needed to model the rapid change in the light curve slope during the energy injection episodes. The shape of the light curve after energy injections is determined by the relativistic aberration of the forward shock light and therefore  $\Theta_0$ . We note that this small value depends on the assumed geometry of the forward shock, here assumed to be isotropic and spherical within the narrow confinement region.

The large energy injections are actually a feature of the energy injection model and these values are compatible with other studies using this model (Thöne et al. 2010, de Ugarte Postigo et al. 2005). For the energy injected to have a visible effect on the light-curve, the energy has to be compatible with the energy in the shock front, leading to an ever increasing energy of the injections. We also note that the total energy budget of the afterglow is highly uncertain, mostly caused by the large uncertainties in the values of  $\epsilon_B$  and  $\epsilon_i$  that require broader energy coverage in the data to be properly constrained.

**Table 5.** Parameters deduced for the energy injection model.

Parameters of the energy injection model		
$E_{\text{total}}$	$1.4^{+45}_{-0.7} \times 10^{50}$ erg	total released energy
$E_0$	$1.5^{+28}_{-1.0} \times 10^{49}$ erg	initially released energy
$E_1$	$2.0^{+2.3}_{-0.9} \times E_0$	energy of the first injection
$t_1$	$22^{+2}_{-3}$ minutes	time of the first injection
$E_2$	$5.7^{+4.4}_{-1.8} \times E_0$	energy of the second injection
$t_2$	$95^{+3}_{-4}$ minutes	time of the second injection
$\Gamma_0$	$77^{+120}_{-28}$	initial outflow Lorentz factor
$n_0$	$29^{+500}_{-28}$ cm $^{-3}$	circumburst medium density
$\Theta_0$	$0.50^{+0.65}_{-0.22}$ deg	initial half-opening angle
$p$	$2.29^{+0.06}_{-0.11}$	electron index
$\epsilon_i$	$0.037^{+0.060}_{-0.035}$	fraction of energy in the lowest-energy electrons
$\epsilon_B$	$2.5^{+16}_{-2.4} \times 10^{-4}$	magnetic energy fraction
$A_V^{\text{host}}$	$0.37^{+0.07}_{-0.09}$	host (MW) extinction

The parameter  $\epsilon_i$  is the fraction of energy in the lowest-energy electrons of the electron population. All times given are in the observer frame relative to the start time of  $t_0 + 170$  s. See Sect. 3.2.3.

Limits on other parameters are found from the general spectral and light curve evolution of the afterglow and are more robust against the assumed start time.

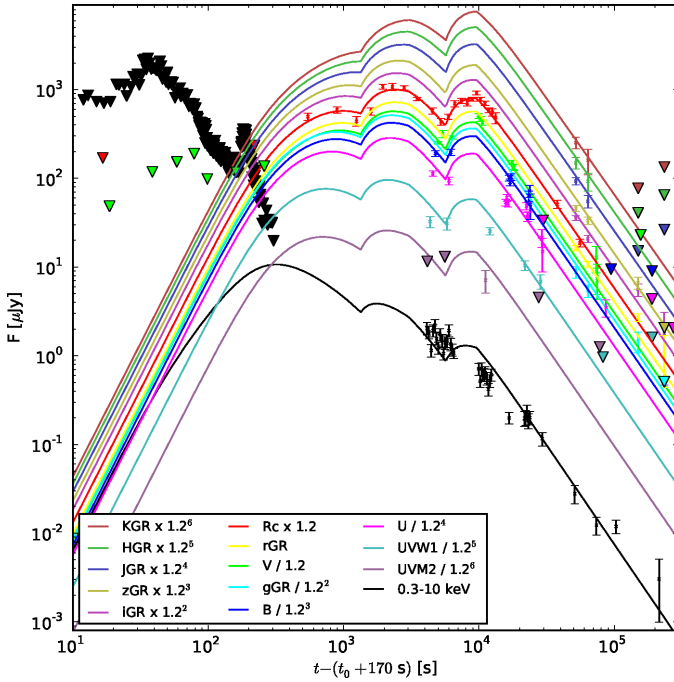


**Fig. 9.** The best fit light curves of the afterglow of GRB 080928. The agreement between the model and the observational data is best if the reference time is shifted by 170 seconds. The parameters of the model are given in Table 5. Filters called “GR” stand for the GROND filter set. Light curves in different bands are arbitrarily shifted for clarity by powers of 1.2.

Finally, could there be a possible contribution from a reverse shock? Basically, there is only one observational constraint (the optical flux) among many parameters that determine the reverse

shock emission. Given that our model requires a substantial energy injection in the forward shock, there could be a substantial optical emission from a long-lived reverse shock. So, there could be a significant contribution to the optical bumps from the reverse shock. In the numerical model we have considered only the forward-shock because that shock is more likely to be the source of the X-ray emission after 10 ks, i.e., when energy injection ceases and the ejecta electrons cool fast enough to yield little X-ray emission. Adding the contribution of the reverse shock(s) to the model might not affect the value we obtained for the jet opening angle.

### 3.3. The isotropic equivalent energy and gamma-ray peak luminosity

Given the results of the spectral fit in the high-energy domain we can estimate the isotropic-equivalent energy released during the prompt emission phase. Fitting the BAT and GBM data for the time of the gamma-ray precursor between 46.5 s and 121 s gives an isotropic equivalent energy of  $E_{\text{iso}}$  (1–10000 keV) =  $(0.40 \pm 0.03) \times 10^{52}$  erg, while a fit of the combined XRT-BAT-GBM data during the main peak emission between  $t_0 + 198.75$  s and  $t_0 + 228.4$  s leads to  $E_{\text{iso}} = (0.88 \pm 0.025) \times 10^{52}$  erg. Fixing the peak energy for the value found in the second interval ( $132^{+49}_{-16}$  keV; Table 1) we find for the whole burst from  $t_0 - 23.5$  s to  $t_0 + 372.5$  s an isotropic energy of  $E_{\text{iso}} = (1.44 \pm 0.92) \times 10^{52}$  erg, in agreement with the Amati relation (Amati 2006).

From the light curve modeling in Sect. 3.2.3 we obtained  $\Theta_0$  and  $E_0$  (the energy in the collimated ejecta; Table 5), so that the isotropic equivalent kinetic energy  $E_{\text{kin,iso}}$  can be calculated. In principle, this, compared to  $E_{\text{iso}}$ , gives the radiative efficiency  $\eta$  in the prompt emission phase,  $\eta = E_{\text{iso}} / (E_{\text{kin,iso}} + E_{\text{iso}})$ . Unfortunately, within the  $1\sigma$  error bars of the model fit the result is not constraining.

The *Fermi*/GBM data allows an estimate of the variability of the light curve, a quantity that has been shown to correlate with the isotropic equivalent peak luminosity,  $L_{\text{iso,peak}}$ . Following the method described in Li & Paczyński (2006) (see also Rizzuto et al. 2007), and using a smoothing time scale of  $t_{50} = 3.3$  s, we derived a variability index of  $V = -2.67$ , which is the normalized squared deviation of the observer-frame light curve from a Savitzky-Golay filtered reference light curve. This results in  $\log L_{\text{iso,peak}} [\text{erg s}^{-1}] = 50.75^{+0.49}_{-0.59}$  (100 keV to 1 MeV, rest frame), about three orders of magnitude less than in the case of the very energetic burst GRB 080916C (Greiner et al. 2009).

### 3.4. The GRB host galaxy

The deep 5th epoch GROND images taken 6.5 months after the burst at a seeing of  $\sim 1''$  do not show any galaxy underlying the position of the optical transient down to the following  $3\sigma$  upper limits (AB magnitudes):  $g' = 25.4$ ,  $r' = 25.6$ ,  $i' = 24.6$ ,  $z' = 24.3$ ,  $J = 22.0$ ,  $H = 21.6$ ,  $K_S = 20.9$ . Assuming for simplicity a power-law spectrum for this galaxy of the form  $F_\nu \propto \nu^{-\beta_{\text{gal}}}$ , for the  $r'$  band this translates into an absolute magnitude of  $M_{r'} = m_{r'} - \mu - k$ , where  $\mu = 45.54$  mag is the distance modulus and  $k$  is the cosmological  $k$ -correction,  $k = -2.5(1 - \beta_{\text{gal}}) \log(1 + z)$ . For a representative value of  $\beta_{\text{gal}} = 1$  this gives a lower limit of  $M_{r'} > -19.94$ , which is in agreement with the luminosities found so far for the GRB host galaxy population. In fact, much less luminous hosts are known (see Savaglio et al. 2009). However, could one of the galaxies seen in projection close to the afterglow be the host?

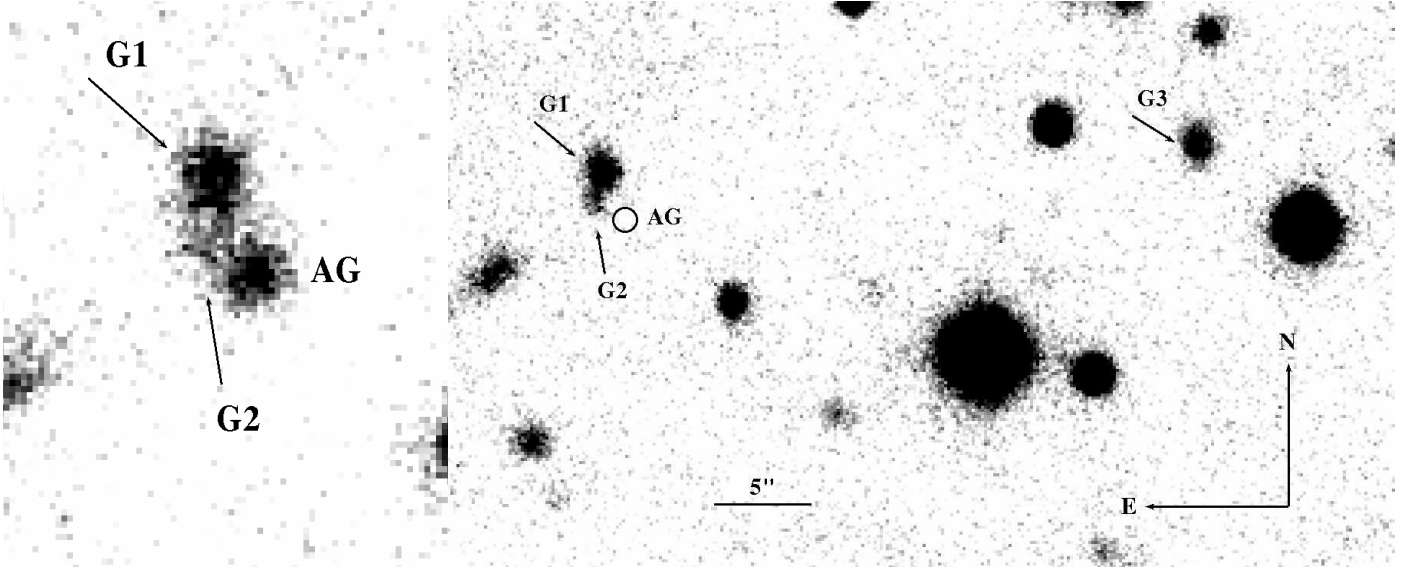


**Fig. 10.** *Left:* Zoom-in of the GROND combined  $g'r'i'z'$ -band image obtained 1.74 days after the burst at a seeing of  $1''.5$ . It shows the afterglow (AG) and the brightest galaxies close to it. *Right:* Zoom-in of the stacked GROND optical  $g'r'i'z'$ -band images obtained on May 15, 2009, 6.5 months after the burst (5th epoch) when the afterglow had faded away. It also shows the galaxy (G3) that was coincidentally covered by the slit of the spectrograph when the redshift of the afterglow was measured with the ESO/VLT (Vreeswijk et al. 2008; Fynbo et al. 2009). Data for G1 to G3 are summarized in Table 6.

Close to the position of the afterglow there is a relatively bright galaxy (labeled G1 in Fig. 10) with  $r' = 23.41 \pm 0.05$ . Using the stacked GROND  $g'r'i'z'$ -band images from the 5th epoch, its central coordinates (Table 6) are offset by  $2''.6 \pm 0''.3$  from the position of the optical afterglow. If this galaxy is at the redshift of the burst, then the projected offset of the optical transient from its centre is  $(22.2 \pm 2.6)$  kpc. This is almost 20 times larger than the median projected angular offset of 1.31 kpc found by Bloom et al. (2002) for a sample of 20 host galaxies of long bursts, making it unlikely that this is the host galaxy of GRB 080928.

Some arcseconds south of G1 lies a diffuse object which could either be physically associated to G1 or represent another foreground/background galaxy. This object (G2 in Fig. 10) is  $1''.5 \pm 0''.3$  away from the afterglow position. If it is at the redshift of the burst, its projected distance from the afterglow is  $(13 \pm 2.6)$  kpc, again hardly in agreement with the observed GRB offset distribution. However, both objects/galaxies are potentially close enough in projection to imprint a signal on the GRB afterglow spectrum. Indeed, Fynbo et al. (2009) report a foreground absorption line system exhibiting several strong Fe, Mg and Ca lines at a redshift of  $z = 0.7359$ . In the  $1''$  slit passing over the afterglow, Fynbo et al. (2009) identify a galaxy  $30''$  away from the afterglow at a redshift of  $z = 0.736$ . This redshift is identical to the value found for the absorbing system (Vreeswijk et al. 2008). We labelled this galaxy as G3.

Using *HyperZ* (Bolzonella et al. 2000), we used our multi-color photometry to obtain the photometric redshift of the galaxies in the field to identify the objects correlated to the absorbing system and the afterglow. The aperture photometry (see Tab. 6) was performed on the GROND seven band images, after correcting for the different PSFs used through PSF-matching techniques using IRAF tasks (see Alcock et al. 1999).

In Table 7, we provide the best fit in terms of  $\chi^2/\text{d.o.f.}$  of the observed broad-band SEDs of G1 to G3 if we fix the redshift of these objects at  $z = 0.736$  (the redshift of the intervening system seen by Fynbo et al. 2009) and at  $z = 1.6919$  (the redshift

of the afterglow). The results indicate that with high probability no one of the galaxies is the host galaxy and that G1 is not the foreground absorber seen in the afterglow spectrum.

For object G3, we find a *HyperZ* solution in very good agreement with the value of  $z = 0.736$  reported by Vreeswijk et al. (2008) ( $\chi^2/\text{d.o.f.} = 1.01$ ). However, the detection in only the four optical bands does not allow us to constrain the dust extinction in this galaxy. Unfortunately, in the case of G2 a *HyperZ* fit with the redshift as a free parameter leads to no conclusive results, the resulting error bars are very large and the photometry can be affected by the nearby galaxy G1. On the other hand, a *HyperZ* fit with the redshift fixed at  $z = 0.736$  gives a reasonable photometric solution ( $\chi^2/\text{d.o.f.} = 1.07$ ; Table 7). This makes it possible that G2 is responsible for the absorption line system seen in the afterglow spectrum, given the proximity of G2 to the spectral slit passing over G3 and the afterglow.

When we treat the redshift as a free parameter, not fixing it to the value of the afterglow or the absorbing system, we find that the best *HyperZ* solution for G1 is  $z = 1.46^{+0.15}_{-0.10}$  (Fig. 11), in both cases (whether we consider G2 to be a separate galaxy or not), confirming that G1 is not related to any other object.

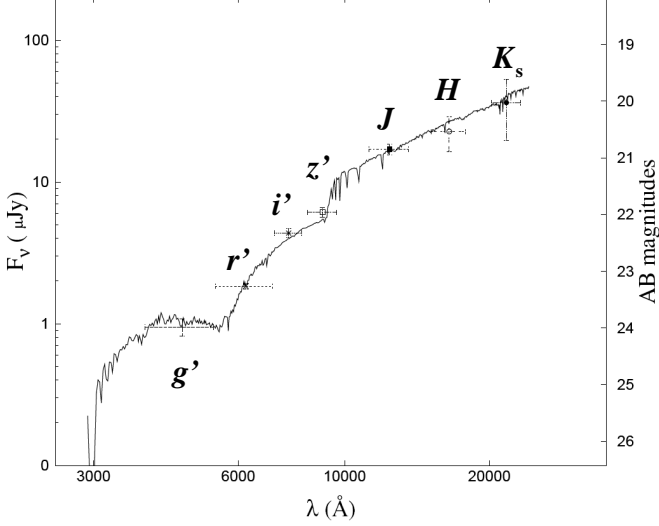
**Table 7.** Results obtained modeling the galaxies SED.

Object	$\chi^2_{0.7359}$	Dust	$A_V^{\text{host}}$	$\chi^2_{1.6919}$	Dust	$A_V^{\text{host}}$
G1 starburst	3.98	LMC	1.0	3.47	SMC	0.8
G2 irregular	1.07	LMC	0.7	3.49	MW	0.8
G3 irregular	1.01	—	0.0	3.76	—	0.0

*HyperZ* results for the fit of the SED of G1, G2, and G3 (using a fixed redshift) based on GROND data obtained 6.5 months after the burst. Also given are the corresponding values for the deduced host extinction  $A_V^{\text{host}}$  and the preferred host extinction law (SMC, LMC, or Milky Way).

**Table 6.** Coordinates and AB magnitudes of objects G1 to G3, not corrected for Galactic extinction.

Object	R.A., Dec. (J2000)	$g'$	$r'$	$i'$	$z'$	$J$	$H$	$K_s$
G1	06:20:16.96, -55:11:56.6	24.22(15)	23.41(05)	22.43(08)	22.03(08)	20.89(09)	20.55(30)	20.00(50)
G2	06:20:16.99, -55:11:58.0	25.20(50)	24.50(06)	23.26(09)	22.70(05)	21.50(20)	21.20(30)	> 20.7
G3	06:20:13.35, -55:11:54.9	23.13(12)	23.12(05)	22.63(07)	22.20(05)	> 22.0	> 21.6	> 20.9

**Fig. 11.** The SED of galaxy G1 close to the afterglow (see Fig. 10), obtained from images taken with GROND 6.5 months after the burst ( $g'r'i'z'JHK_s$  filters). Shown is the best *HyperZ* fit that is based on the template of a dusty starburst galaxy at a redshift of  $z=1.46$  (see also Table 7).

#### 4. Summary

GRB 080928 was a long burst lasting for about 400 seconds. It was detected by *Swift*/BAT and *Fermi*/GBM and was well followed-up by *Swift*/XRT and *Swift*/UVOT. Ground-based follow up observations were performed by the robotic ROTSE-IIIa telescope in Australia and the multi-channel imager GROND on La Silla. Its early X-ray light curve is dominated by two bright peaks that occurred within the first 400 seconds after the BAT trigger. The first peak is delayed by some seconds from the gamma-ray peak emission, while the second peak has no obvious counterpart in the high-energy band. It occurred when the gamma-ray emission had already faded away. After a data gap between about 400 s and 4 ks, the X-ray light curve continued to show evidence for small-scale fluctuations, while between 200 s and 10 ks the optical light curve shows bumps and dips, possibly related to energy injections into the forward shock (refreshed shocks).

Between about 200 s and 400 s after the BAT trigger, *Swift*/UVOT together with ROTSE-IIIa detected optical emission and *Swift*/XRT monitored X-ray radiation while the GRB was still emitting in the gamma-ray band. The combination of these data allowed us to construct the SED from about 1 eV to 150 keV at several epochs, making GRB 080928 one of the rare cases where a spectral energy distribution spanning from optical to gamma rays can be traced during the prompt emission. The first epoch covers the main peak emission in gamma-rays as well as in the X-ray band. The resulting SED can be understood as due to synchrotron radiation with a break energy around 4 keV.

In addition, the optical and X-ray data allowed us to check if the radiation following the first strong peak seen in the X-ray light curve is due to large-angle emission (the peak itself might have a different origin). Taking into account the observed rising optical emission contemporaneous to the decaying X-ray tail, we found that the data can be understood only if one of the assumptions made in the LAE model is relaxed, namely the assumption that the electron population is the same at all angles  $\theta$ . This implies the use of a generalized version of the LAE model, for which we obtain the flux and the energy of the peak evolving as  $F_p \propto \theta^{-2-a}$  and  $E_p \propto \theta^{-1-b}$ , with  $a = -1.2 \pm 0.2$ , and  $b = 1.1 \pm 0.5$ . Those dependencies reflect the distribution with angle of the ejecta parameters that determine  $F_p$  and  $E_p$ , such as ejecta kinetic energy per solid-angle or the bulk Lorentz factor.

The X-ray data can be best fit assuming an effective hydrogen column density in the host of  $N_H^{\text{host}} = 3.6_{-2.2}^{+1.8} \times 10^{21} \text{ cm}^{-2}$ . For a Milky Way interstellar medium this would imply a host extinction of  $A_V^{\text{host}} = 2_{-1.2}^{+1.0} \text{ mag}$ , in contrast to  $A_V^{\text{host}} = 0.12 \pm 0.03 \text{ mag}$  found in the optical afterglow data, which indeed seem to favor a Milky Way interstellar extinction law. The fact that the dust-to-gas ratio is relatively small along GRB sight-lines in their host galaxies is a well-known phenomenon, possibly due to dust destruction by the intense fireball light.

In our interpretation of the data the first peak in the optical light curve at  $\sim 1$  ks is the onset of the afterglow and the following two bumps at  $\sim 2$  ks and  $\sim 10$  ks are caused by energy injections. Applying an energy injection model, the analysis explains the data after 10 ks with a post-jet evolution requiring a small opening angle ( $\lesssim 1.0$  degree).

The optical afterglow was found to be about  $2''.6$  south of a relatively bright face-on galaxy, with unknown redshift. However, its photometric redshift based on GROND  $g'r'i'z'JHK_s$  data is in disagreement with the redshift of the afterglow found by Fynbo et al. (2009). In addition, the angular offset of the afterglow from this galaxy, corresponding to about 22 kpc at a redshift of  $z=1.69$ , disfavours its identification as the GRB host. Since no galaxy underlying the position of the afterglow could be detected, only deep flux limits for its host galaxy could be obtained. No other host galaxy candidate could be identified. However, given the redshift of the burst, this is not remarkable and matches well into the ensemble properties of the luminosities of GRB host galaxies found so far (Savaglio et al. 2009).

GRB 080928 has shown once more the tremendous amount of information that can be gathered for a single burst and the fundamental importance of timely responses as well as the joint analysis of all the available data. It is the combination of gamma-ray, X-ray, and optical/NIR data that characterizes once more the golden age of GRB research.

**Acknowledgements.** The authors thank the anonymous referee for a very constructive report. A. Rossi and S.K. acknowledge support by DFG grant K1 766/11-3 and AR additionally from the BLANCEFLOR Boncompagni-Ludovisi, née Bildt foundation. S.S., D.A.K. and P.F. acknowledge support by the Thüringer Landessternwarte Tautenburg, Germany, as well as DFG grant K1 766/16-1. T.K. acknowledges support by the DFG cluster of excellence ‘Origin and Structure of the Universe’. S.S. acknowledges further support by a Grant of

Excellence from the Icelandic Research Fund. A. Rossi acknowledges Sandra Savaglio, Daniele Pierini and Cristiano Guidorzi for helpful discussions. A. Rau and S.K. acknowledge Re'em Sari for helpful remarks. D.A.K. acknowledges A. Zeh for fitting scripts. Part of the funding for GROND (both hardware as well as personnel) was generously granted from the Leibniz-Prize to Prof. G. Hasinger (DFG grant HA 1850/28-1). This work made use of data supplied by the UK Swift Science Data Centre at the University of Leicester.

## References

- Achterberg, A., Gallant, Y. A., Kirk, J. G., & Guthmann, A. W. 2001, *MNRAS*, 328, 393
- Alcock, C., Allsman, R. A., Alves, D., et al. 1999, *ApJ*, 521, 602
- Amati, L. 2006, *MNRAS*, 372, 233
- Atwood, W. B., Abdo, A. A., Ackermann, M., et al. 2009, *ApJ*, 697, 1071
- Band, D., Matteson, J., Ford, L., et al. 1993, *ApJ*, 413, 281
- Barthelmy, S. D., Barbier, L. M., Cummings, J. R., et al. 2005, *Space Sci. Rev.*, 120, 143
- Beuermann, K., Hessman, F. V., Reinsch, K., et al. 1999, *A&A*, 352, L26
- Blackburn, J. K. 1995, in *Astronomical Society of the Pacific Conference Series*, Vol. 77, *Astronomical Data Analysis Software and Systems IV*, ed. R. A. Shaw, H. E. Payne, & J. J. E. Hayes, 367
- Blake, C. H., Bloom, J. S., Starr, D. L., et al. 2005, *Nature*, 435, 181
- Bloom, J. S., Kulkarni, S. R., & Djorgovski, S. G. 2002, *AJ*, 123, 1111
- Bolzonella, M., Miralles, J.-M., & Pelló, R. 2000, *A&A*, 363, 476
- Burrows, D. N., Hill, J. E., Nousek, J. A., et al. 2005a, *Space Sci. Rev.*, 120, 165
- Burrows, D. N., Romano, P., Falcone, A., et al. 2005b, *Science*, 309, 1833
- Butler, N. R. & Kocevski, D. 2007, *ApJ*, 663, 407
- Cardelli, J. A., Clayton, G. C., & Mathis, J. S. 1989, *ApJ*, 345, 245
- Cash, W. 1979, *ApJ*, 228, 939
- Cenko, S. B., Kelemen, J., Harrison, F. A., et al. 2009, *ApJ*, 693, 1484
- Chincarini, G., Mao, J., Margutti, R., et al. 2010, *MNRAS*, 406, 2113
- Chincarini, G., Moretti, A., Romano, P., et al. 2007, *ApJ*, 671, 1903
- Chornock, R., Cenko, S. B., Griffith, C. V., et al. 2009, *GCN Circ.*, 8291
- Cummings, J., Barthelmy, S. D., Baumgartner, W., et al. 2008, *GCN Circ.*, 8294
- Curran, P. A., Evans, P. A., de Pasquale, M., Page, M. J., & van der Horst, A. J. 2010, *ApJ*, 716, L135
- de Ugarte Postigo, A., Castro-Tirado, A. J., Gorosabel, J., et al. 2005, *A&A*, 443, 841
- Elíasdóttir, Á., Fynbo, J. P. U., Hjorth, J., et al. 2009, *ApJ*, 697, 1725
- Evans, P. A., Beardmore, A. P., Page, K. L., et al. 2009, *MNRAS*, 397, 1177
- Evans, P. A., Beardmore, A. P., Page, K. L., et al. 2007, *A&A*, 469, 379
- Falcone, A. D., Morris, D., Racusin, J., et al. 2007, *ApJ*, 671, 1921
- Fenimore, E., Barthelmy, S. D., Baumgartner, W., et al. 2008, *GCN Circ.*, 8297
- Fenimore, E. & Sumner, M. 1997, in *All-Sky X-ray Observations in the Next Decade*, ed. M. Matsuoka & N. Kawai, 167
- Ferrero, A., French, J., & Melady, G. 2008, *GCN Circ.*, 8303
- Fruchter, A., Krolík, J. H., & Rhoads, J. E. 2001, *ApJ*, 563, 597
- Fynbo, J. P. U., Jakobsson, P., Prochaska, J. X., et al. 2009, *ApJ*, 697, 526
- Galama, T. J. & Wijers, R. A. M. J. 2001, *ApJ*, 549, L209
- Gehrels, N., Chincarini, G., Giommi, P., et al. 2004, *ApJ*, 611, 1005
- Giuliani, A., Mereghetti, S., Fornari, F., et al. 2008, *A&A*, 491, L25
- Goldoni, P., Flores, H., Malesani, D., et al. 2010, *GCN Circ.*, 8301
- Greiner, J., Bornemann, W., Clemens, C., et al. 2008, *PASP*, 120, 405
- Greiner, J., Bornemann, W., Clemens, C., et al. 2007, *The Messenger*, 130, 12
- Greiner, J., Clemens, C., Krühler, T., et al. 2009, *A&A*, 498, 89
- Jóhannesson, G. 2006, PhD thesis, University of Iceland
- Jóhannesson, G., Björnsson, G., & Gudmundsson, E. H. 2006, *ApJ*, 647, 1238
- Kalberla, P. M. W., Burton, W. B., Hartmann, D., et al. 2005, *A&A*, 440, 775
- Kann, D. A., Klose, S., & Zeh, A. 2006, *ApJ*, 641, 993
- Kann, D. A., Klose, S., Zhang, B., et al. 2010, *ApJ*, 720, 1513
- Kirk, J. G., Guthmann, A. W., Gallant, Y. A., & Achterberg, A. 2000, *ApJ*, 542, 235
- Klotz, A., Gendre, B., Stratta, G., et al. 2008, *A&A*, 483, 847
- Krimm, H. A., Granot, J., Marshall, F. E., et al. 2007, *ApJ*, 665, 554
- Krühler, T., Greiner, J., McBreen, S., et al. 2009, *ApJ*, 697, 758
- Krühler, T., Küpcü Yoldaş, A., Greiner, J., et al. 2008, *ApJ*, 685, 376
- Kuin, N. P. M., Sakamoto, T., & Holland, S. 2008, *GCN Circ.*, 8298
- Kumar, P. & Granot, J. 2003, *ApJ*, 591, 1075
- Kumar, P. & Panaitescu, A. 2000, *ApJ*, 541, L51
- Li, L.-X. & Paczyński, B. 2006, *MNRAS*, 366, 219
- Liang, E. W., Zhang, B., O'Brien, P. T., et al. 2006, *ApJ*, 646, 351
- Madau, P. 1995, *ApJ*, 441, 18
- Meegan, C., Lichti, G., Bhat, P. N., et al. 2009, *ApJ*, 702, 791
- Osborne, J. P., Beardmore, A. P., Evans, P. A., & Goad, M. R. 2008, *GCN Circ.*, 8295
- Paciesas, B., Briggs, M., & Preece, R. 2008, *GCN Circ.*, 8316
- Page, K. L., Willingale, R., Osborne, J. P., et al. 2007, *ApJ*, 663, 1125
- Panaiteanu, A. & Kumar, P. 2000, *ApJ*, 543, 66
- Pérez-Ramírez, D., de Ugarte Postigo, A., Gorosabel, J., et al. 2010, *A&A*, 510, 105
- Perley, D. A., Bloom, J. S., & Prochaska, J. X. 2008a, *GCN Circ.*, 7791
- Perley, D. A., Li, W., Chornock, R., et al. 2008b, *ApJ*, 688, 470
- Piran, T. 2005, *Reviews of Modern Physics*, 76, 1143
- Quimby, R. M., Rykoff, E. S., Yost, S. A., et al. 2006, *ApJ*, 640, 402
- Racusin, J. L., Liang, E. W., Burrows, D. N., et al. 2009, *ApJ*, 698, 43
- Rau, A., Kienlin, A. V., Hurley, K., & Lichti, G. G. 2005, *A&A*, 438, 1175
- Rhoads, J. E. 1999, *ApJ*, 525, 737
- Rizzuto, D., Guidorzi, C., Romano, P., et al. 2007, *MNRAS*, 379, 619
- Romano, P., Campana, S., Chincarini, G., et al. 2006, *A&A*, 456, 917
- Roming, P. W. A., Kennedy, T. E., Mason, K. O., et al. 2005, *Space Sci. Rev.*, 120, 95
- Roming, P. W. A., Koch, T. S., Oates, S. R., et al. 2009, *ApJ*, 690, 163
- Rossi, A., Clemens, C., Greiner, J., et al. 2008a, *GCN Circ.*, 8296
- Rossi, A., de Ugarte Postigo, A., Ferrero, P., et al. 2008b, *A&A*, 491, L29
- Rykoff, E. S., Yuan, F., & McKay, T. A. 2008, *GCN Circ.*, 8293
- Sakamoto, T., Barthelmy, S. D., Evans, P. A., et al. 2008, *GCN Circ.*, 8292
- Savaglio, S., Glazebrook, K., & LeBorgne, D. 2009, *ApJ*, 691, 182
- Schady, P., Mason, K. O., Page, M. J., et al. 2007, *MNRAS*, 377, 273
- Schady, P., Page, M. J., Oates, S. R., et al. 2010, *MNRAS*, 401, 2773
- Schlegel, D. J., Finkbeiner, D. P., & Davis, M. 1998, *ApJ*, 500, 525
- Shen, R. & Zhang, B. 2009, *MNRAS*, 398, 1936
- Spergel, D. N., Verde, L., Peiris, H. V., et al. 2003, *ApJ*, 593, 148, 175
- Starling, R. L. C., van der Horst, A. J., Rol, E., et al. 2008, *ApJ*, 672, 433
- Starling, R. L. C., Wijers, R. A. M. J., Wiersema, K., et al. 2007, *ApJ*, 661, 787
- Stratta, G., Fiore, F., Antonelli, L. A., Piro, L., & De Pasquale, M. 2004, *ApJ*, 608, 846
- Tavani, M., Barbiellini, G., Argan, A., et al. 2009, *A&A*, 502, 995
- Thöne, C. C., Kann, D. A., Jóhannesson, G., et al. 2010, *A&A*, 523, A70
- Tody, D. 1993, in *Astronomical Society of the Pacific Conference Series*, Vol. 52, *Astronomical Data Analysis Software and Systems II*, ed. R. J. Hanisch, R. J. V. Brissenden, & J. Barnes, 173
- Vaughan, S., Goad, M. R., Beardmore, A. P., et al. 2006, *ApJ*, 638, 920
- Vestrand, W. T., Wozniak, P. R., Wren, J. A., et al. 2005, *Nature*, 435, 178
- Vestrand, W. T., Wren, J. A., Wozniak, P. R., et al. 2006, *Nature*, 442, 172
- Vianello, G., Götz, D., & Mereghetti, S. 2009, *A&A*, 495, 1005
- Vreeswijk, P., Malesani, D., Fynbo, J., et al. 2008, *GCN Circ.*, 8301
- Warmels, R. H. 1992, in *Astronomical Society of the Pacific Conference Series*, Vol. 25, *Astronomical Data Analysis Software and Systems I*, ed. D. M. Worrall, C. Biemesderfer, & J. Barnes, 115
- Watson, D., Hjorth, J., Fynbo, J. P. U., et al. 2007, *ApJ*, 660, L101
- Wilms, J., Allen, A., & McCray, R. 2000, *ApJ*, 542, 914
- Winkler, C., Courvoisier, T., Di Cocco, G., et al. 2003, *A&A*, 411, L1
- Xu, D., Fynbo, J. P. U., Tanvir, N. R., et al. 2009, *GCN Circ.*, 10053
- Zhang, B. & Mészáros, P. 2004, *Int. J. Mod. Phys. A*, 19, 2385

## Appendix A: The data set

Table A.1. Log of the ROTSE-IIIa telescope observations.

Time (days)	Time (s)	$T_{start}$ (s)	$T_{stop}$ (s)	CR Magnitude
0.002160	186.7	132.0	263.9	> 18.5
0.004509	389.6	272.8	556.3	$18.38 \pm 0.22$
0.008266	714.2	565.6	901.8	$17.35 \pm 0.10$
0.012341	1066.3	911.2	1247.7	$17.16 \pm 0.09$
0.016375	1414.8	1256.7	1592.9	$17.48 \pm 0.13$
0.020442	1766.2	1602.1	1947.2	$17.20 \pm 0.10$
0.024512	2117.8	1956.1	2293.0	$16.50 \pm 0.06$
0.028530	2465.0	2302.2	2639.3	$16.51 \pm 0.10$
0.034383	2970.7	2648.7	3331.8	$16.54 \pm 0.06$
0.042429	3665.9	3340.8	4022.6	$16.85 \pm 0.05$
0.054459	4705.3	4373.1	5062.8	$17.18 \pm 0.08$
0.062571	5406.2	5071.8	5762.6	$17.49 \pm 0.10$
0.070628	6102.2	5771.4	6452.0	$17.35 \pm 0.08$
0.078676	6797.6	6461.6	7151.1	$16.99 \pm 0.09$
0.087760	7582.5	7160.1	8029.8	$16.90 \pm 0.07$
0.096907	8372.8	8038.5	8720.9	$16.96 \pm 0.08$
0.104911	9064.3	8729.8	9411.6	$16.85 \pm 0.05$
0.112957	9759.5	9420.7	10110.5	$16.68 \pm 0.06$
0.121012	10455.4	10119.7	10802.3	$16.86 \pm 0.05$
0.130107	11241.2	10811.6	11687.9	$16.97 \pm 0.06$
0.139266	12032.6	11696.8	12378.0	$17.17 \pm 0.07$
0.147299	12726.6	12386.8	13075.8	$17.22 \pm 0.10$
0.155384	13425.2	13084.4	13774.8	$17.38 \pm 0.15$

Magnitudes are Vega magnitudes (unfiltered  $R$ -equivalent data, see Quimby et al. 2006), not corrected for Galactic extinction (Sect. 2.3). Midtimes have been derived logarithmically.

Table A.2. Log of the *Swift*/UVOT observations.

Time (days)	Time (s)	$T_{start}$ (s)	$T_{stop}$ (s)	Magnitude	Filter
0.001909	164.9	160.4	169.7	> 17.1	<i>v</i>
0.002184	188.7	179.0	199.0	> 19.7	<i>white</i>
0.002416	208.7	199.0	219.0	$19.03 \pm 0.25$	<i>white</i>
0.002648	228.7	219.0	239.0	$18.70 \pm 0.21$	<i>white</i>
0.002879	248.8	239.0	259.0	$18.44 \pm 0.17$	<i>white</i>
0.003110	268.7	259.0	278.7	$19.29 \pm 0.31$	<i>white</i>
0.003834	331.2	285.0	385.0	$19.15 \pm 0.41$	<i>v</i>
0.004969	429.3	385.0	478.7	$18.96 \pm 0.39$	<i>v</i>
0.050063	4325.4	4226.7	4426.5	> 19.1	<i>uvm2</i>
0.052440	4530.8	4432.0	4631.8	$18.02 \pm 0.15$	<i>uvw1</i>
0.054817	4736.2	4637.3	4837.1	$17.54 \pm 0.07$	<i>u</i>
0.057191	4941.3	4842.5	5042.2	$18.05 \pm 0.08$	<i>b</i>
0.059573	5147.1	5048.2	5247.9	$17.96 \pm 0.04$	<i>white</i>
0.061956	5353.0	5254.0	5453.8	> 19.3	<i>uvm2</i>
0.064332	5558.3	5459.3	5659.1	$17.66 \pm 0.10$	<i>v</i>
0.066706	5763.4	5664.3	5864.1	> 19.0	<i>uvm2</i>
0.069081	5968.6	5869.6	6069.3	$18.07 \pm 0.15$	<i>uvw1</i>
0.071451	6173.4	6074.3	6274.1	$17.74 \pm 0.11$	<i>u</i>
0.073834	6379.2	6280.1	6479.9	$18.02 \pm 0.08$	<i>b</i>
0.076205	6584.1	6485.0	6684.7	$17.81 \pm 0.05$	<i>white</i>
0.078267	6762.3	6690.7	6834.6	> 18.8	<i>uvm2</i>
0.117545	10155.9	10007.1	10306.9	$17.16 \pm 0.07$	<i>v</i>
0.121060	10459.6	10310.8	10610.6	$17.24 \pm 0.06$	<i>v</i>
0.124573	10763.1	10614.3	10914.0	$17.34 \pm 0.07$	<i>v</i>
0.131495	11361.1	10920.2	11819.9	$19.66 \pm 0.28$	<i>uvm2</i>
0.141377	12214.9	11826.8	12615.8	$18.28 \pm 0.10$	<i>uvw1</i>
0.184457	15937.1	15787.9	16087.7	$18.35 \pm 0.09$	<i>u</i>
0.187971	16240.7	16091.5	16391.3	$18.21 \pm 0.09$	<i>u</i>
0.191485	16544.3	16395.1	16694.9	$18.38 \pm 0.09$	<i>u</i>
0.195021	16849.8	16700.6	17000.3	$18.74 \pm 0.08$	<i>b</i>
0.198535	17153.4	17004.2	17304.0	$18.87 \pm 0.09$	<i>b</i>
0.202048	17456.9	17307.7	17607.5	$18.71 \pm 0.09$	<i>b</i>
0.205580	17762.1	17612.9	17912.6	$18.51 \pm 0.06$	<i>white</i>
0.209096	18065.9	17916.6	18216.4	$18.64 \pm 0.06$	<i>white</i>
0.211904	18308.5	18220.2	18397.2	$18.65 \pm 0.09$	<i>white</i>
0.254794	22014.2	21568.9	22468.7	$19.25 \pm 0.13$	<i>uvw1</i>
0.261860	22624.7	22475.3	22775.1	$18.45 \pm 0.10$	<i>u</i>
0.265374	22928.4	22779.0	23078.7	$18.75 \pm 0.12$	<i>u</i>
0.268888	23231.9	23082.5	23382.3	$18.74 \pm 0.13$	<i>u</i>
0.272424	23537.4	23388.0	23687.8	$19.25 \pm 0.14$	<i>b</i>
0.275939	23841.1	23691.7	23991.5	$19.11 \pm 0.16$	<i>b</i>
0.278780	24086.6	23995.4	24178.3	$19.49 \pm 0.30$	<i>b</i>
0.321708	27795.5	27349.3	28249.1	> 20.2	<i>uvm2</i>
0.332203	28702.3	28256.0	29155.7	$19.71 \pm 0.18$	<i>uvw1</i>
0.339259	29312.0	29162.5	29462.3	$19.34 \pm 0.23$	<i>u</i>
0.342773	29615.6	29466.1	29765.8	$19.73 \pm 0.37$	<i>u</i>
0.345653	29864.5	29770.2	29959.0	> 18.9	<i>u</i>
0.385349	33294.2	33157.3	33431.6	> 19.6	<i>uvm2</i>
0.841783	72730.0	46011.4	114964.1	> 21.9	<i>uvm2</i>
0.853404	73734.1	46917.8	115877.5	$21.14 \pm 0.31$	<i>v</i>
0.903886	78095.7	52273.5	116673.6	> 21.5	<i>uvm2</i>
0.954216	82444.2	56280.7	120770.5	> 21.8	<i>uvw1</i>
1.005800	86901.3	62061.1	121684.1	$21.31 \pm 0.22$	<i>u</i>
1.095660	94665.0	73622.3	121722.0	> 21.3	<i>b</i>
0.864812	74719.8	74534.4	74905.6	$21.85 \pm 0.36$	<i>white</i>
0.864400	74684.2	74534.4	74834.2	$21.73 \pm 0.34$	<i>white</i>
1.811460	156510.0	121764.2	201170.5	> 20.5	<i>v</i>
2.194020	189563.0	178401.4	201423.3	> 21.1	<i>u</i>
2.196340	189764.0	178556.9	201674.8	> 21.4	<i>b</i>
2.199990	190079.0	178715.3	202165.7	> 21.3	<i>uvw1</i>
3.177100	274501.0	260418.7	289345.7	> 21.9	<i>u</i>

Magnitudes are Vega magnitudes, not corrected for Galactic extinction (Sect. 2.3). Midtimes have been derived logarithmically.



**Table A.3.** Log of the GROND multi-color observations.

Time (days)	Filter	Exposure (s)	Brightness (mag <sub>AB</sub> )
0.6031	<i>g'r'i'z'</i>	12 × 370	21.40 ± 0.15 / 21.03 ± 0.07 / 20.54 ± 0.07 / 20.43 ± 0.08
0.6031	<i>JHK<sub>S</sub></i>	240 × 10	19.83 ± 0.10 / 19.49 ± 0.15 / 19.11 ± 0.15
0.7398	<i>g'r'i'z'</i>	12 × 370	21.93 ± 0.16 / 21.48 ± 0.08 / 21.13 ± 0.10 / 20.78 ± 0.10
0.7398	<i>JHK<sub>S</sub></i>	360 × 10	20.40 ± 0.16 / 20.01 ± 0.22 / 19.60 ± 0.30
1.7370	<i>g'r'i'z'</i>	12 × 370	23.35 ± 0.25 / 22.99 ± 0.10 / 22.56 ± 0.16 / 22.53 ± 0.16
1.7370	<i>JHK<sub>S</sub></i>	360 × 10	> 21.8 / > 20.9 / > 20.4
2.708	<i>g'r'i'z'</i>	4 × 370	> 24.3 / 23.41 ± 0.40 / 23.35 ± 0.73 / > 23.2
2.708	<i>JHK<sub>S</sub></i>	120 × 10	> 21.2 / > 20.4 / > 19.8
201	<i>g'r'i'z'</i>	12 × 370	> 25.4 / > 25.6 / > 24.6 / > 24.3
201	<i>JHK<sub>S</sub></i>	360 × 10	> 22.0 / > 21.6 / > 20.9

The first column provides the midtime in days after the onset of the burst. The last (5th) epoch data were used to characterize the field galaxy population and to set constraints on the magnitudes of a galaxy close to the optical/NIR afterglow. Magnitudes are given in the AB photometric system, not corrected for Galactic extinction (Sect. 2.3). Midtimes have been derived logarithmically.

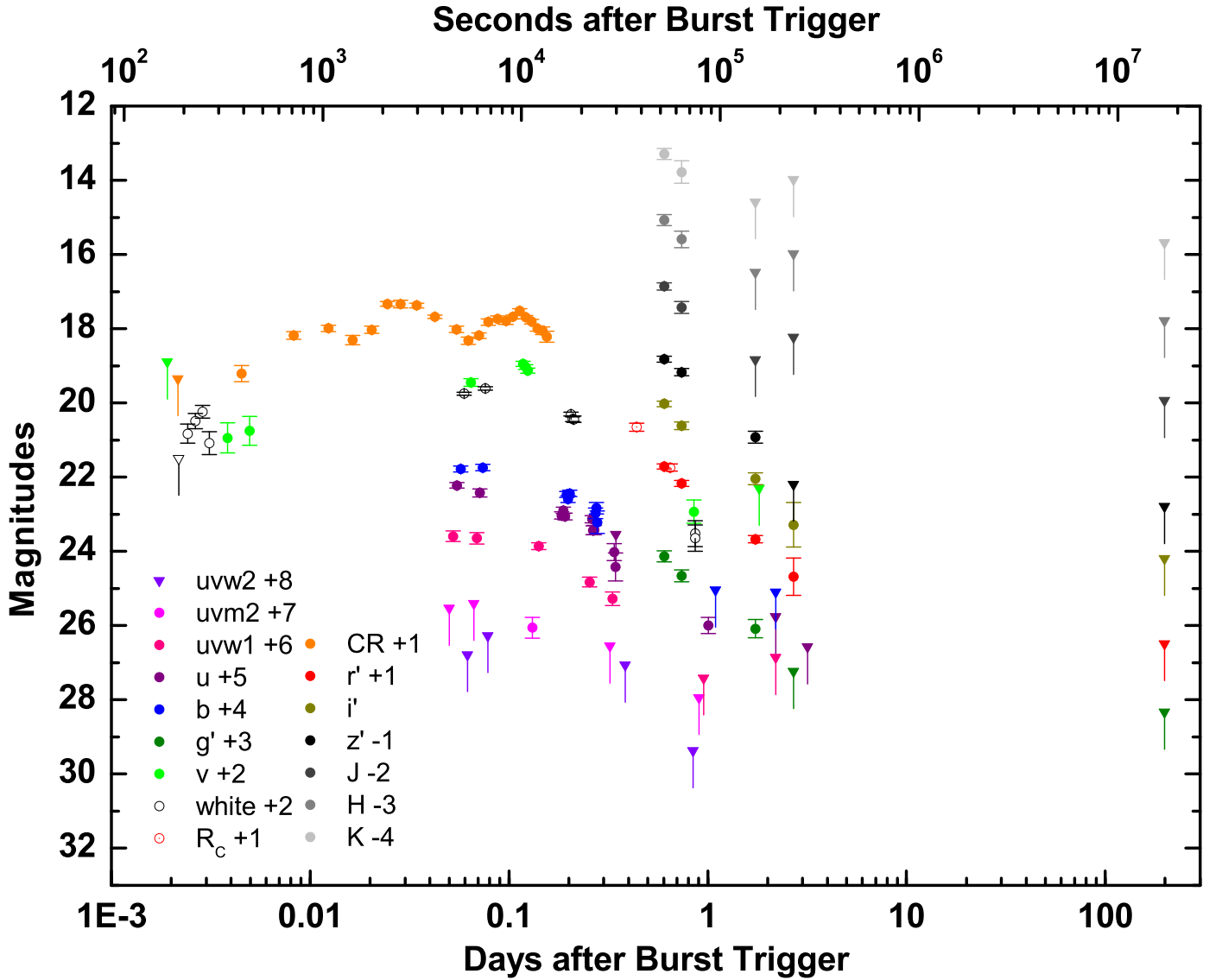


**Fig. A.1.** The complete optical/NIR data set of the afterglow of GRB 080928 as it is listed in Tables A.1, A.2, and A.3. All magnitudes are given in the Vega system, and the GROND magnitudes are corrected according Greiner et al. (2008). Colors have been shifted by the values given in the legend for clarity. Downward pointing triangles are upper limits, *uvw2* was the only filter in which only upper limits could be derived.



**Table A.4.** Secondary standard stars within 4 arcmin of the afterglow position (Fig. 2).

#	R.A., Dec. (J2000)	$g'$	$r'$	$i'$	$z'$	$J$	$H$	$K_s$
1	06:20:15.23 -55:12:45.4	14.426(01)	13.727(01)	13.269(01)	13.102(01)	12.753(01)	12.613(02)	12.880(02)
2	06:20:13.45 -55:12:32.5	19.427(05)	18.987(05)	18.593(05)	18.478(08)	18.267(05)	18.219(10)	18.435(23)
3	06:20:13.87 -55:12:17.1	17.291(01)	16.982(01)	16.709(01)	16.668(02)	16.568(03)	16.673(03)	16.780(07)
4	06:20:14.65 -55:12:01.1	17.513(02)	17.366(02)	17.103(02)	17.072(03)	16.988(03)	17.100(03)	17.208(10)
5	06:20:12.70 -55:11:55.1	20.734(14)	19.460(08)	18.017(03)	17.450(04)	16.886(03)	16.778(04)	16.853(07)
6	06:20:12.21 -55:11:45.9	18.307(02)	18.061(03)	17.734(03)	17.643(04)	17.508(04)	17.509(05)	17.711(23)
7	06:20:14.51 -55:11:45.1	19.989(08)	18.962(05)	18.204(04)	17.946(05)	17.561(03)	17.341(05)	17.378(11)
8	06:20:06.18 -55:12:02.1	20.499(05)	19.456(03)	18.453(03)	18.077(02)	17.598(06)	17.353(08)	17.556(05)
9	06:19:58.96 -55:12:57.4	17.430(03)	17.413(02)	17.206(02)	17.185(01)	17.123(04)	17.312(07)	17.553(07)
10	06:19:58.75 -55:10:40.3	19.275(03)	18.121(02)	17.026(02)	16.613(01)	16.110(05)	16.022(05)	16.143(02)
11	06:19:56.64 -55:09:57.4	20.949(14)	20.212(14)	19.672(13)	19.389(14)	18.794(08)	18.609(12)	18.403(13)
12	06:20:16.00 -55:10:28.9	18.087(03)	17.755(02)	17.442(03)	17.370(01)	17.168(05)	17.218(06)	17.313(04)

Calibration of the field in  $JHK_s$  was performed using 2MASS stars. The magnitudes of the selected 2MASS stars were then transformed into the GROND filter system and finally into AB magnitudes using  $J(AB) = J(Vega) + 0.91$ ,  $H(AB) = H(Vega) + 1.38$ ,  $K_s(AB) = K_s(Vega) + 1.79$  (Greiner et al. 2008). Numbers in parentheses give the photometric  $1\sigma$  statistical uncertainty of the secondary standards in units of milli-mag.